*J. Fluid Mech.* (2005), *vol.* 528, *pp.* 173–205.  
doi:10.1017/S0022112004003258 Printed in the United Kingdom

# A stochastic model for high-Rayleigh-number convection

By SCOTT WUNSCH AND ALAN R. KERSTEIN

Combustion Research Facility, Sandia National Laboratories, Livermore, CA 94551-0969, USA

(Received 16 May 2002 and in revised form 28 September 2004)

A stochastic one-dimensional model for thermal convection is formulated and applied to high-Rayleigh-number convection. Comparisons with experimental data for heat transfer in Rayleigh–Bénard cells are used to estimate two model parameters. Reasonable agreement with experimental results is obtained over a wide range of physical parameter values (six orders of magnitude in Rayleigh number, five orders of magnitude in Prandtl number). Using the model, the statistics of fluctuations in the core of the convection cell are studied. Good agreement with available experimental data is obtained. Two distinct p.d.f. shapes are seen; one at low Prandtl number which matches experimental observations, and another at high Prandtl number for which no experimental data exists. The model results are interpreted in terms of two distinct mechanisms for the production of core fluctuations.

## 1. Introduction

Turbulent thermal convection has long been recognized as an important aspect of many natural fluid systems, with examples coming from both astrophysics (stars) and geophysics (Earth's atmosphere and molten interior). The physics of thermal convection has typically been studied experimentally using Rayleigh–Bénard systems, in which a cylinder of fluid is heated from below. The resulting temperature contrast in the fluid generates turbulent motions which transport heat from the lower plate to the upper plate of the cell. The long history of both experimental and theoretical investigations of this system is summarized in Siggia (1994).

The driving force in convective turbulence is the temperature difference $\Delta T$ between the top and bottom plates, which induces a density contrast $\Delta\rho = \beta\Delta T$ for thermal expansion coefficient $\beta$. In the Boussinesq approximation assumed here, temperature and density variations are proportional and the density difference across the cell is much smaller than the average fluid density $\rho_0$. The strength of the driving force is expressed in dimensionless form by the Rayleigh number $Ra$, defined as

$$Ra \equiv \frac{g\Delta\rho\Lambda^3}{\rho_0\nu\kappa} = \frac{g\beta\Delta T\Lambda^3}{\rho_0\nu\kappa}, \tag{1.1}$$

where $g$ is the acceleration due to gravity, $\Lambda$ is the distance separating the walls, $\nu$ is the kinematic viscosity, and $\kappa$ is the molecular diffusivity. Two other parameters also govern the behaviour of the system. One is the Prandtl number, $Pr \equiv \nu/\kappa$, which measures the relative strengths of the molecular processes. It is determined by the choice of working fluid. The other is the aspect ratio of the cell; the ratio of cell diameter (assuming a cylindrical cell) to cell height. Natural systems might be considered to correspond to infinite aspect ratio cells, although in many natural

systems the upper or lower boundaries may also differ from fixed-temperature plates. The most often measured quantity in convective cells is the heat transfer rate, which is expressed in dimensionless terms by the Nusselt number $Nu$, defined as the ratio of the turbulent heat transfer at the plates to the hypothetical heat transfer in quiescent fluid owing to molecular conduction. The classical assumption that the heat transfer should be independent of the height $\Lambda$ for large $Ra$ yields the scaling

$$Nu \sim Ra^{1/3}, \tag{1.2}$$

based on dimensional analysis (Siggia 1994). Experimental results in Rayleigh–Bénard cells generally indicate scaling laws with exponents less than 1/3, with the actual value depending on $Pr$. A scaling analysis proposed by Grossmann & Lohse (2000, 2001, 2002) attempts to explain these non-classical scaling laws by considering the dissipation of energy and thermal fluctuations in the cell.

Although much attention has been paid to understanding the non-classical behaviour of the heat transfer, the turbulent fluctuations of the temperature in the core of the Rayleigh–Bénard cell are also of interest and are the primary focus of this study. The typical magnitude of the temperature fluctuations has been observed to scale with $Ra$ (Castaing *et al.* 1989; Niemela *et al.* 2000). The magnitude also shows a dependence on cell geometry, although the probability density function (p.d.f.) of the fluctuations does not (Daya & Ecke 2001). Understanding how the shape of the p.d.f. depends on physical flow parameters and boundaries is important for generalizing experimental observations to natural convecting systems in geophysics and astrophysics. Knowing the likelihood of large temperature fluctuations is especially important in reacting flows, since reaction rates have a strongly nonlinear temperature dependence.

In this work, a stochastic one-dimensional model is used to study high-Rayleigh-number convection. The model is a version of the 'One-Dimensional Turbulence' (ODT) model created by Kerstein (1999) and has been previously applied to stably stratified turbulence (Wunsch & Kerstein 2001; Wunsch 2003). Comparisons with heat transfer measurements in Rayleigh–Bénard cells are performed to set parameters and validate the performance of the model. Since the one-dimensional model cannot reproduce the important effects of cell geometry and sidewall heat loss, perfect agreement with experiment is not expected. Instead, the goal is to reproduce the approximate $Nu$ at a given $Ra$ and $Pr$ so that the correct flow conditions are obtained to permit study of the interior fluctuations. Unlike simple scaling theories, the stochastic time-dependent nature of this model allows a detailed study of the statistics of fluctuations in the core of the cell. These data are compared with experimentally measured statistics (where available) and provide insight into the convection processes that govern the likelihood of fluctuations.

The advantages and disadvantages of this modelling approach relative to other forms of numerical simulation are worth mentioning. First and foremost, the restriction to one dimension makes the model much more computationally affordable than direct numerical simulation. This makes it possible to explore the parameter space of $Ra$ and $Pr$ much more efficiently. Published studies of the Prandtl-number dependence of the heat transfer rate using direct numerical simulation have been performed only at the modest Rayleigh numbers of $Ra = 10^6$ (Verzicco & Camussi 1999) and $Ra = 10^7$ (Kerr & Herring 2000), while exploration of the dependence on $Ra$ at near-unity Prandtl number has reached $Ra = 2 \times 10^9$ (Verzicco 2002). This last study required a total of $1.6 \times 10^6$ mesh nodes, while our model simulations of the same case require only $1.6 \times 10^4$ mesh nodes. The ODT simulations are also carried

out for much longer times to collect accurate statistical information on temperature fluctuations ($10^3$ to $10^5$ large-eddy turnover times, compared to 20 to 100 turnover times for typical direct numerical simulations). Of course, the advantage of full three-dimensional numerical simulation is that all relevant effects, including geometry and sidewall heat transfer, are captured, which is not the case in the model. However, these effects are negligible in many natural systems, and the ODT model therefore might be well-suited to future studies of those flows.

A more efficient approach to simulating the effects of geometry on a convecting flow is the use of large-eddy simulation (Kimmel & Domaradzki 2000) or LES, which neglects the smaller scales. However, this technique does not allow the study of small-scale fluctuations. The model used in this work is therefore complementary to large-eddy simulation, in the sense that LES incorporates geometry, but parameterizes the effects of small-scale fluctuations, whereas the opposite is true of ODT.

## 2. One-dimensional model

### 2.1. *Overview*

The temperature structure of a convecting system is a function primarily of the vertical coordinate $y$. Hence, it is plausible that a one-dimensional model might describe the physics of the problem. The approach used here is a version of the ODT model created by Kerstein (1999); the specific version is identical to that applied to stably stratified turbulence in Wunsch & Kerstein (2001) and Wunsch (2003), except for the boundary conditions and forcings. Only a brief summary of the model will be presented here; see the earlier literature for additional details.

Two scalar fields, each a function of vertical position $y$ and time $t$, are used to describe convecting systems in this model. One is a density scalar, defined as $\delta\rho(y,t) \equiv \rho(y,t) - \rho_0$, which represents a vertical profile of density fluctuations in the convective cell. The reference density $\rho_0$ is taken to be the fluid density at the lower plate, so that $\delta\rho \geqslant 0$. In the Boussinesq approximation, we could equivalently use a temperature variable $\delta T$, such that $\delta T/\Delta T = \delta\rho/\Delta\rho$. However, for consistency with previous ODT publications in which temperature was not the only source of density fluctuations, we formulate the model in terms of $\delta\rho$ in this work. The other scalar field in the model is 'velocity', $v(y,t)$, whose square represents a vertical profile of kinetic energy in the cell. It is not a real velocity in the sense that it does not directly advect itself or the density scalar. Rather, it is used simply as a kinetic-energy surrogate in the model. Consequently, it is most plausibly interpreted in the current context as representing the magnitude of velocity fluctuations within the cell.

In ODT, advection consists of randomly chosen measure-preserving mapping events that rearrange the scalar fields. Each mapping is a local event, with a well-defined position $y_0$ and spatial extent $l$, and each event is loosely interpreted as corresponding to a turbulent 'eddy' of size $l$ in the flow. Mappings are possible on all scales and represent all scales of convective motions. The mappings are responsible for all advective transport within the model. (Recall that the velocity scalar does not directly advect fluid.) Mappings on the largest scale (order $\Lambda$) therefore simulate the transport resulting from large-scale motions, while smaller mappings simulate the transport resulting from smaller-scale turbulent eddies within the cell. The mapping function is designed to 'wrinkle' the flow, reducing length scales within the affected interval. In addition, the mappings induce net scalar transport in the presence of a gradient. The times and locations of the mapping events are selected at random from

a rate distribution whose functional dependence on the local ODT variables $\delta\rho(y,t)$ and $v(y,t)$ is based on the energetics of turbulence.

Using simple energetic scaling arguments, a characteristic frequency can be inferred for each possible eddy in the system, thereby determining an event rate distribution corresponding to the current state of the system. The model then randomly samples all possible eddies with the assigned frequencies. During the time intervals between these instantaneous mappings, the scalar fields evolve according to the molecular transport equations:

$$\left(\partial_t - \nu\partial_y^2\right)v(y,t) = 0, \tag{2.1}$$

$$\left(\partial_t - \kappa\partial_y^2\right)\delta\rho(y,t) = 0. \tag{2.2}$$

Boundary conditions are applied at the top ($y=\Lambda$) and bottom ($y=0$) of the cell, so that $v(y=0)=v(y=\Lambda)=0$, $\delta\rho(y=0)=0$ and $\delta\rho(y=\Lambda)=\Delta\rho$. These equations are solved as a time sequence of initial-value problems, each starting immediately after a mapping event and proceeding until the time of the next mapping event.

It is worth clarifying the interpretation of the velocity scalar and the mappings with regard to the large-scale convection rolls (or 'wind') which are observed in turbulent Rayleigh–Bénard cells. Since the ODT velocity scalar serves only as a kinetic energy reservoir, it is interpreted in this work as representing velocity fluctuations within the cell, but not large-scale coherent motions. While the latter have no explicit representation within the model, it is plausible that the vertical transport which results from these motions in a real cell are represented with some accuracy in the model by the large-scale mappings. The non-classical heat transfer results presented in § 4.1 are an indication that the effective transport of the large-scale motions in a Rayleigh–Bénard cell is represented with some fidelity in the model.

The ODT model contains four basic elements necessary for exploring turbulent convecting flows: energy conservation, scalar transport, multiscale dynamics and molecular dissipation. The restriction to one computational dimension makes it possible to efficiently study a wider range of parameter space than is possible by direct numerical simulation.

### 2.2. *Eddy definition*

The fundamental dynamical object in the model is the advective mapping. It consists of a measure-preserving map $f(y)$ of the domain onto itself, so that any scalar field undergoes the transformation $v(y)\rightarrow v(f(y))$ when acted on by the map. The mapping acts on a segment of length $l$, from position $y_0$ to $y_0+l$. It is loosely interpreted as representing the effects of an 'eddy' of size $l$ on the scalar fields. The velocity and density scalars are both mapped to mimic the transport of fluid elements. The particular mapping function is arbitrary, but we choose a piecewise-linear function as a convenient way of meeting the requirements of measure preservation and finite extent. As in previous ODT work, we use a three-piece function which takes the line segment, shrinks it to a third of its original length, and then places three copies on the original domain. The middle copy is reversed, so that the mapped field $v(f(y))$ is continuous if $v(y)$ is continuous. The mapping function reduces to the identity map $f(y)=y$ outside of the mapped interval. Details of the function $f(y)$ can be found in Kerstein (1999).

The rearrangement of the density field by the mapping alters the total potential energy, but the mapping itself leaves the total kinetic energy unchanged. To enforce energy conservation, a function $K(y)$ of specified form is added to the velocity field whenever an eddy occurs. The mapping induces displacements $y-f(y)$. This is a

natural candidate for the energy exchange function, so we assume $K(y) = y - f(y)$. This function is non-zero only within the mapped region.

Thus, under the action of an eddy, the density and velocity fields undergo the transformations

$$\left.\begin{aligned} &\delta\rho(y) \to \delta\rho(f(y)), \\ &v(y) \to v(f(y)) + cK(y). \end{aligned}\right\} \tag{2.3}$$

The amplitude $c$ of the energy exchange term $cK(y)$ is determined for each eddy individually to achieve energy conservation. The eddy therefore converts all potential energy released by the mapping to kinetic energy within the mapping interval.

To calculate $c$, the energetic consequences of applying (2.3) must be assessed. The energy $E$ is defined as

$$E \equiv \tfrac{1}{2}\rho_0 \int v^2(y)\mathrm{d}y + g \int \delta\rho(y) y \mathrm{d}y. \tag{2.4}$$

To achieve energy conservation, the amplitude $c$ in (2.3) must be determined so that the energy is unchanged by the action of the eddy. This yields

$$c = \frac{27}{4l}\left(-v_K \pm \sqrt{v_K^2 - \frac{8}{27}\frac{\rho_K}{\rho_0} gl}\right), \tag{2.5}$$

where

$$s_K \equiv \frac{4}{9l^2}\int_{y_0}^{y_0+l} s(y)[l - 2(y - y_0)]\mathrm{d}y, \tag{2.6}$$

and $s$ denotes either $v$ or $\rho$. The numerical factors in (2.5) and (2.6) are determined by the precise mathematical form of the mapping function, and are required to achieve energy conservation for each eddy mapping. The solution (2.5) is not necessarily real; mappings that do not yield a real value for $c$ are assumed to be energetically prohibited (more details later). The solution branch is chosen so that $c = 0$ if $\rho_K = 0$. This implies using the '+' sign in (2.5) whenever $v_K > 0$, and the '−' sign otherwise. There is an ambiguity if $v_K = 0$ that is resolved using a random perturbation procedure. Using the value of $c$ given by (2.5) for each mapping event, $cK(y)$ is added to $v$ after the mapping to conserve energy.

### 2.3. *Eddy selection*

The final ingredient required in the model is to determine the time sequence of eddies, each parameterized by position $y_0$ and size $l$. To estimate a time scale for each possible eddy, consider the Sharp–Wheeler turnover time $\tau(y_0, l; t)$ for eddies driven by an unstable density difference $\hat{\rho}$: $\tau \sim \sqrt{l\rho_0/(g\hat{\rho})}$. In real turbulence, this is roughly the time required for a region of size $l$ to convectively mix. In ODT, eddies are implemented instantaneously, but eddies in a given order-one range of size and location should occur approximately once each turnover time. In ODT, $\tau$ is determined by analogy with the Sharp–Wheeler time, but expressed in terms of energy by assuming that $(l/\tau)^2$ is proportional to the potential energy change $(-8gl\rho_K/27\rho_0)$ due to the mapping:

$$\left(\frac{l}{\tau}\right)^2 \sim -\frac{8}{27}\frac{\rho_K}{\rho_0} gl. \tag{2.7}$$

This time scale is equivalent (up to numerical factors) to the time required for a fluid element with density contrast $\rho_K$ to fall (drag-free) a distance $l$ through surrounding fluid with density $\rho_0$.

While density fluctuations are the primary drivers of eddy turnovers in the flows considered here, kinetic energy also contributes. The typical turnover time for eddies in the absence of density differences scales as $\tau(l) \sim l/\tilde{v}(l)$, where $\tilde{v}(l)$ is some measure of the velocity fluctuations. A convenient velocity measure for determining the turnover time for individual eddies is $v_K$, defined by (2.6). Both density and velocity contributions must be included in determining the eddy turnover times. While the precise functional form is arbitrary, we choose a linear combination of the form

$$\left(\frac{l}{\tau}\right)^2 \sim v_K^2 - \frac{8}{27}\frac{\rho_K}{\rho_0} g l - Z\frac{\nu^2}{l^2} \tag{2.8}$$

for consistency with the ODT energy conservation mechanism (2.5). Eddies whose $\tau$ values are imaginary are, of course, prohibited by energetic considerations. The third term on the right-hand side of (2.8) is included to prohibit eddies smaller than the viscous damping scale from occurring. It is negligible at larger scales. The constant of proportionality $Z$ in the viscous damping term is a parameter of the model.

The time scales $\tau$ for all possible eddies are translated into an eddy-rate distribution $\lambda$, defined as $\lambda(y_0, l; t) \equiv C/l^2\tau(y_0, l; t)$. All of the interesting physics is subsumed in $\tau$ (2.8), while the dimensionless constant $C$ is a parameter of the model. Using the turnover time in (2.8), the eddy-rate distribution is given by

$$\lambda = \frac{C\nu}{l^4}\sqrt{\left(\frac{v_K l}{\nu}\right)^2 - \frac{8g}{27\nu^2}\frac{\rho_K}{\rho_0} l^3 - Z}. \tag{2.9}$$

The actual rate of an eddy with position between $y_0$ and $y_0 + \mathrm{d}y_0$ and length in the range between $l$ and $l + \mathrm{d}l$ is given by $\lambda(y_0, l)\,\mathrm{d}y_0\,\mathrm{d}l$. We can see that, in the absence of gravity, a 'local Reynolds number', $v_K l/\nu$, determines the rate of each eddy. Buoyant forces either enhance or lower the effective local Reynolds number. The construction of the ODT eddy rate given above uses two free parameters, $C$ and $Z$. The overall rate parameter $C$ determines the strength of the turbulence in the model, while $Z$ determines the smallest eddy size (analogous to the Kolmogorov scale in the model).

The model is basically an application of mixing length theory locally throughout the model domain, defining a wide range of possible mixing lengths $l$ and corresponding time scales $\tau$ that depend on the current local flow structure as well as on $l$. Turbulent mixing is randomly applied throughout the system on all length scales based on the locally appropriate time scales.

Given initially motionless fluid and an initially constant density gradient $\Delta\rho/\Lambda$ in the cell, the measure of the density fluctuations that drive an eddy of size $l$ is $\rho_K = -2\Delta\rho l/27\Lambda$. Hence, an eddy of size $l$ yields a real value of $\lambda$ based on (2.9) only if $Ra \geqslant (27/4)^2 Z Pr(\Lambda/l)^4$. Since the ODT model is based on turbulence scalings, it makes sense only when applied to problems in which the Rayleigh number is large enough to permit a range of eddy sizes to occur. A rough estimate of this condition is obtained by requiring $\lambda$ to be real for eddies of size $l \sim 0.1\Lambda$ in the initial configuration. This yields

$$Ra \geqslant 10^5 Z Pr \tag{2.10}$$

as the approximate condition for well-developed turbulence in the model. This sets a threshold value of $Ra$ for turbulent convection at any given $Pr$ in the model. Although ODT will yield results at lower values of $Ra$, their validity would be suspect since the cascade assumption of ODT will be violated whenever (2.10) does not hold.

### 2.4. *Conservation laws*

Because the eddies do not alter the energy in the system, boundaries and viscous dissipation are the only sources of energy change. Using the differential equations for the dissipative processes, it is straightforward to form an equation for the energy change:

$$\partial_t E = g\kappa \int y\partial_y^2 \delta\rho \mathrm{d}y + \nu\rho_0 \int v\partial_y^2 v \mathrm{d}y = g\kappa\Delta\rho \left( \frac{\Lambda}{\Delta\rho} \partial_y \delta\rho|_{y=\Lambda} - 1 \right) - \nu\rho_0 \int (\partial_y v)^2 \mathrm{d}y. \tag{2.11}$$

The rate of energy change jumps instantaneously when an eddy occurs, but the total energy itself is not changed by the eddy. In a statistical steady state, the energy change is, on average, zero ($\langle \partial_t E \rangle = 0$), and this implies the relation

$$Ra(Nu - 1) = Pr^2 \epsilon, \tag{2.12}$$

where the Nusselt number $Nu$ is defined as

$$Nu \equiv \frac{\Lambda}{\Delta\rho} \langle \partial_y \delta\rho(y) \rangle|_{y=\Lambda} \tag{2.13}$$

and the dimensionless energy dissipation $\epsilon$ is

$$\epsilon \equiv \frac{\Lambda^3}{\nu^2} \int \langle (\partial_y v)^2 \rangle \mathrm{d}y. \tag{2.14}$$

There is an additional conservation law for the density variance, $\delta\rho^2$. Since eddies preserve all moments of the density field, only the boundaries and molecular dissipation alter the variance. Again, it is straightforward to form the conservation law

$$\partial_t \int \delta\rho^2 \mathrm{d}y = 2\kappa \int \delta\rho \left( \partial_y^2 \delta\rho \right) \mathrm{d}y = 2\kappa (\delta\rho \partial_y \delta\rho)|_0^\Lambda - 2\kappa \int (\partial_y \delta\rho)^2 \mathrm{d}y. \tag{2.15}$$

In statistical steady state this implies

$$\epsilon_\rho \equiv \frac{\Lambda}{\Delta\rho^2} \int \langle (\partial_y \delta\rho)^2 \rangle \mathrm{d}y = Nu. \tag{2.16}$$

The conservation relations (2.12) and (2.16) are the one-dimensional analogues of the general conservation laws for three-dimensional convection (Siggia 1994).

## 3. Numerical implementation

To render the ODT model in non-dimensionalized form for numerical simulation, it is necessary to rescale the length, time, velocity and density variables by reference values. The obvious length scale for rescaling is the cell height $\Lambda$. The dimensionless position $y'$ and eddy size $l'$ are defined by $y' \equiv y/\Lambda$ and $l' \equiv l/\Lambda$. Time is rescaled in terms of the time scale for viscous smoothing of cell-scale structures: $t' \equiv t\nu/\Lambda^2$.

The velocity is rescaled in terms of $y'/t'$: $v' \equiv Cv\Lambda/\nu$. Owing to the inclusion of $C$ in the dimensionless velocity, physical velocities are rescaled from model velocities by the model constant $C$. The time evolution equation for the velocity field becomes

$$\frac{\partial v'}{\partial t'} = \frac{\partial^2 v'}{\partial y'^2}. \tag{3.1}$$

The density field $\delta\rho$ is non-dimensionalized by the density difference $\Delta\rho$ across the cell: $\delta\rho' \equiv \delta\rho/\Delta\rho$. The time evolution equation for the density field is

$$\frac{\partial \delta\rho'}{\partial t'} = \frac{1}{Pr}\frac{\partial^2 \delta\rho'}{\partial y'^2}, \tag{3.2}$$

where $Pr \equiv \nu/\kappa$ is the Prandtl number.

The rescaled eddy rate is

$$\lambda' = \frac{1}{l'^4}\sqrt{(l'v'_K)^2 - g'\rho'_K l'^3 - ZC^2}, \tag{3.3}$$

where the dimensionless gravity is $g' \equiv (8C^2\Delta\rho\Lambda^3/27\rho_0\nu^2)g$. The dimensionless measure of velocity and density fluctuations is

$$s'_K \equiv \frac{4}{9l'^2}\int_{y'_0}^{y'_0+l'} \mathrm{d}y' s'(y')(l' - 2(y' - y'_0)), \tag{3.4}$$

where $s$ denotes $v$ or $\rho$, and the dimensionless energy-exchange amplitude (2.5) is

$$c' = \frac{27}{4l'}\left(-v'_K \pm \sqrt{v'^2_K - g'\rho'_K l'}\right). \tag{3.5}$$

The ODT model now contains a single meaningful model parameter $ZC^2$, as well as the physical control parameters $g'$ and $Pr$. As a result of this particular non-dimensionalization, only the combination of model parameters $ZC^2$ need be varied in exploring the parameter space. For any given $ZC^2$, a number of simulations with different $g'$ and $Pr$ can be performed, and the heat transfer rates ($Nu$) calculated for each case. Selection of plausible individual values of $C$ and $Z$ requires empirical input. Experimental data for $Nu(Ra, Pr)$ is required to estimate the value of $Ra$ that corresponds to the $Nu$ calculated for one simulation. Once this is known, a plausible value for $C$ can be calculated from the definition of $g'$, re-expressed as

$$C^2 = \frac{27}{8Ra}Prg'. \tag{3.6}$$

Once $C$ has been estimated, the value of $Ra$ for each simulation with the same $ZC^2$ can be calculated from the values of $g'$ and $Pr$ corresponding to that simulation. This procedure is employed in the next section to estimate $C$.

In the absence of empirical input, each ODT simulation with particular values of $ZC^2$, $g'$ and $Pr$ corresponds to a family of model solutions with different values of $C$ and $Ra$, so long as $RaC^2$ remains fixed according to (3.6). The quantity $RaC^2$ can therefore be thought of as an 'ODT Rayleigh number', and the scaling of computed quantities (such as $Nu$) with $RaC^2$ can be studied in the model without empirical input, although the prefactor in the scaling relation cannot be compared to experiment unless an empirical estimate of $C$ is made.

The ODT model consists of the continuous implementation of molecular processes based on (3.1) and (3.2) for the velocity and density fields, punctuated by discrete advection events (eddies). Eddies are randomly selected with rates given by (3.3) and (3.4). Details of the sampling process can be found in Kerstein (1999). All eddy sizes (from the grid resolution to the entire cell height) and locations are sampled, but (3.3) determines which are implemented in a grid-independent manner. When an eddy is implemented, both fields are advected by the mapping function, and then $c'K(y')$ is added to the velocity field (to conserve energy), where the amplitude $c'$ is given by (3.5).

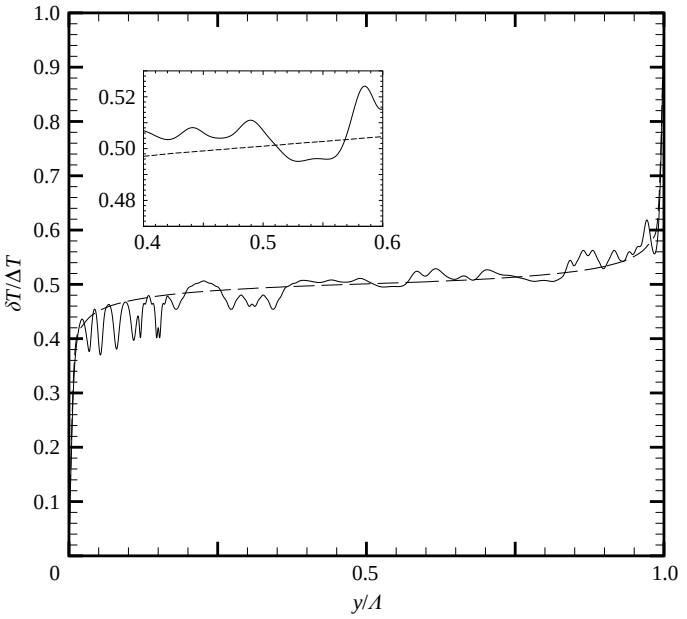


FIGURE 1. Typical ODT instantaneous (solid line) and time-averaged (dashed line) temperature profiles, taken from a simulation with $RaC^2 = 10^{12}$, $Pr = 0.7$, and $ZC^2 = 10^5$. A plausible value of $C$ for this case is $C^2 = 1500$, based on comparisons to experimental data (see figure 4), which corresponds to $Ra = 7 \times 10^8$. Inset: A closeup of the temperature profile near the cell centre.

In numerical implementation, a first-order implicit finite-difference scheme was applied for solution of the molecular process equations. The continual rearrangement of the fields by eddies eliminates any need for sophisticated numerical techniques, since more accurate information is naturally destroyed by the random motions. Grid resolution was sufficient so that the smallest eddy size was 24 to 1000 times the grid point separation, depending on the Prandtl number. Up to 65 536 grid points were used. Simulations were run until a statistically steady state was achieved before any data collection was undertaken.

## 4. Simulation results

Figure 1 shows the temperature profile $\delta T(y)$ resulting from a typical simulation. The profile indicates two thermal boundary regions near $y \sim 0$ and $y \sim \Lambda$, separated by a core mixed region. (For the purpose of presenting results, we use temperature instead of density as our variable, since that is standard in the experimental convection literature which we use for comparison. The two are related according to $\delta T/\Delta T = \delta\rho/\Delta\rho$.) The instantaneous profile shows a number of significant fluctuations; in the time-averaged profile these are smoothed away. The Nusselt number is calculated using the slopes of the averaged profile at the upper and lower plates. Statistics of the temperature and velocity fluctuations are sampled in the well-mixed core region.

The ODT model has no explicit mechanism for representing sidewalls, and conceptually seems most comparable to the infinite-aspect-ratio limit. Vertical motions of all sizes in ODT have the same dynamical form (the eddy mapping). However, in low-aspect-ratio (tall and thin) cells, large vertical motions are influenced by the

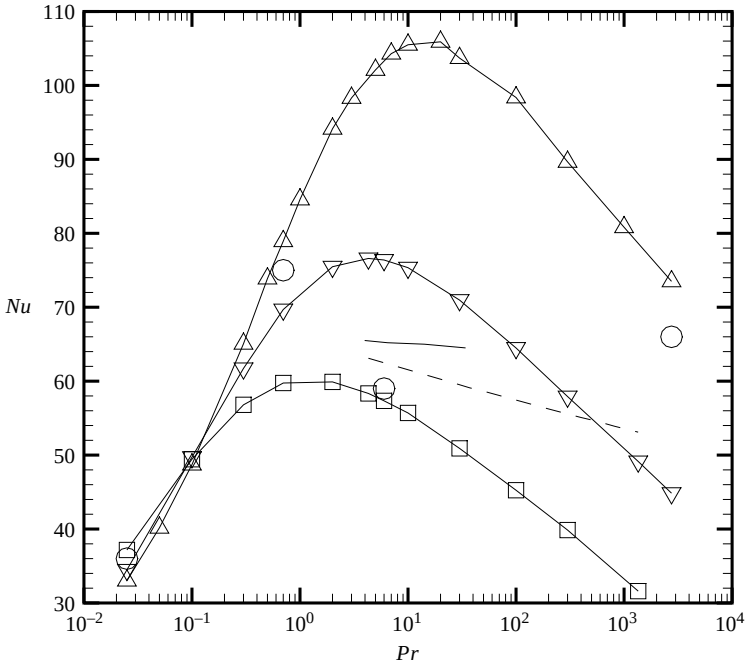


FIGURE 2. *Nu* as a function of *Pr* from ODT simulations with $Ra = 10^9$. Three values of the model constant $ZC^2$ are shown: △, $ZC^2 = 823$; ▽, $10^4$; □, $10^5$. For comparison, experimental data (circles) are shown for mercury ($Pr = 0.025$), helium ($Pr = 0.7$), water ($Pr = 4$), and electrochemical convection ($Pr = 2750$). Also shown are experimental data using different fluids to cover a range of *Pr* in the same apparatus, from Ahlers & Xu (2001) (solid line) and Xia *et al.* (2002) (dashed line).

presence of the sidewalls, while smaller motions in the interior of the cell are not. On the other hand, in large-aspect-ratio cells and in many geophysical and astrophysical convection problems, vertical motions as large as the cell height can occur in the cell interior with minimal influence from the sidewalls. In this case, all dynamical length scales are free from sidewall distortion, which is analogous to ODT. Hence, the model has no way to represent the geometry dependence that has recently been reported for low-aspect-ratio convection cells (Daya & Ecke 2001). In addition, the model lacks any representation of the consequences of imperfectly insulating sidewalls, whose effects may play a significant role in Rayleigh–Bénard cells (Roche *et al.* 2001; Verzicco 2002). Variations in the way in which this effect is accounted for by different groups unfortunately complicates the interpretation of experimental heat transfer measurements (Ahlers & Xu 2001). However, in the absence of data from true infinite-aspect-ratio flows, heat transfer measurements from finite cells are used to estimate plausible values of the model parameters $C$ and $ZC^2$. The goal is not to explain the observed values of *Nu*, but rather to ensure that reasonable heat transfer rates are produced by the simulations to facilitate proper study of the core fluctuations.

### 4.1. *Heat transfer, Nu*(*Ra*, *Pr*)

To illustrate the role of the model parameters $ZC^2$ and $C$, simulations with a range of Prandtl numbers were performed at a Rayleigh number of $Ra = 10^9$ for three different values of $ZC^2$: 823, $10^4$ and $10^5$. The results are shown in figure 2, along

| $ZC^2$ | 823 | $10^4$ | $10^5$ |
|---|---|---|---|
| $C^2$ | 800 | 1200 | 1500 |
| $Z$ | 1.03 | 8.33 | 66.7 |

TABLE 1. Values of $C^2$ and $Z$ selected to match the heat transfer rate in liquid mercury convection at $Ra = 10^9$ for each choice of $ZC^2$.

with a number of experimental results. The value of $C$, which essentially shifts the curves vertically (by changing the physical $Ra$ which corresponds to a given model parameter $RaC^2$) was chosen so that the ODT data would approximately match the experimental point shown at $Pr = 0.025$ (liquid mercury convection). Actual values are shown in table 1. The required value of $C$ changes only modestly because, at low $Pr$, the heat transfer rate becomes independent of viscosity and hence independent of the viscous cutoff parameter $Z$. We can see that the curve $Nu(Pr)$ peaks at a value of $Pr$ which depends on the ODT parameter $ZC^2$, and that for larger Prandtl numbers the heat transfer varies strongly with $Z$, since viscosity is a significant factor in the limit $Pr \to \infty$. The peak value occurs at approximately $Pr \sim 20$ for $ZC^2 = 823$, $Pr \sim 5$ for $ZC^2 = 10^4$, and $Pr \sim 2$ for $ZC^2 = 10^5$. The precise location of the peak of $Nu(Pr)$ is not clear from the experimental data; however, numerical simulations by Kerr & Herring (2000) suggest that it occurs near $Pr = 2$ for $Ra = 10^7$. At large $Pr$, the trend of $Nu$ decreasing as $Pr$ increases seen in the experiments of Ahlers & Xu (2001) and Xia, Lam & Zhou (2002) also appears in the ODT data, although the rate of decrease is slightly larger in the model.

A number of experimental results are shown in figure 2 for comparison to the ODT data. In all cases, values of $Nu$ were estimated from published scaling laws which approximate the original data, which was not available in the literature. All of the data shown were taken in cylindrical convection cells with aspect ratios of either 0.5 or 1.0. Changes in the aspect ratio modestly influence the value of $Nu$, as discussed in Wu & Libchaber (1992). A brief discussion of the source of each of these results is included below.

Sodium is the fluid with the lowest Prandtl number ($Pr = 0.005$) yet attained in a convection cell (Horanyi, Krebs & Muller 1999). However, the highest $Ra$ achieved ($5 \times 10^6$) is too low for direct comparison with other, higher $Pr$ experiments at the same $Ra$. It is therefore not included in figure 2. However, ODT simulations of the $Ra = 5 \times 10^6$ case with the three choices of $ZC^2$ and $C$ given in table 1 give Nusselt numbers in the range of $Nu = 5.1$ to 5.2, which compares favourably to the experimental result of $Nu = 5.3$.

Liquid mercury has the lowest Prandtl number ($Pr = 0.025$) for which a Rayleigh number of $10^9$ has been achieved. Cioni, Ciliberto & Sommeria (1997) report an approximate scaling law $Nu = 0.14Ra^{0.26}$ in a unit aspect ratio cell over the range $5 \times 10^6 \leqslant Ra \leqslant 5 \times 10^9$. This experiment suggests $Nu \simeq 30$ at $Ra = 10^9$. Takeshita *et al.* (1996) report a scaling of $Nu = 0.155Ra^{0.27}$ in the range $10^6 \leqslant Ra \leqslant 10^8$, which extrapolates to a significantly higher value of $Nu \simeq 40$ at $Ra = 10^9$. Hence, figure 2 presents the average ($Nu = 35$) of these two experiments. The earlier results of Rossby (1969) are neglected because the maximum $Ra$ achieved in that work was only $5 \times 10^5$.

In recent years, there have been many experimental studies of helium convection ($Pr \simeq 0.7$) in cells with various aspect ratios. The work of Niemela *et al.* (2000) indicates an approximate scaling of $Nu = 0.124Ra^{0.309}$ over the enormous scaling

range $10^6 \leqslant Ra \leqslant 10^{17}$, yielding an approximate value of $Nu \simeq 75$ at $Ra = 10^9$. This is a different scaling exponent from the previous work of Castaing *et al.* (1989), which reports $Nu = 0.17Ra^{0.29}$ for $Ra$ up to $10^{14}$, also for an aspect ratio 0.5 cell. However, the actual $Nu$ value at $Ra = 10^9$ is $Nu \simeq 69$ in the earlier work, which is only an 8% discrepancy. It is asserted in Niemela *et al.* (2000) that this difference is due to inaccuracies in the properties of helium used to analyse the earlier results. Other results for helium convection report approximate values of $Nu$ at $Ra = 10^9$ of $Nu \simeq 80$ (Wu & Libchaber 1992), $Nu \simeq 75$ (Chavanne *et al.* 1997), and $Nu \simeq 70$ (Chavanne *et al.* 2001). Figure 2 therefore shows $Nu = 75$ for helium convection, representing a number of experiments which indicate that $Nu$ lies in the range $70 - 80$ at $Ra = 10^9$.

Several older experiments have studied convection in water ($Pr \simeq 6$) cells (Garon & Goldstein 1973; Goldstein & Tokuda 1980; Tanaka & Miyata 1980). They cover relatively limited ranges of $Ra$ (typically only two orders of magnitude), including $Ra = 10^9$. Reported scaling results for large-aspect-ratio experiments are $Nu = 0.13Ra^{0.293}$ (Garon & Goldstein 1973) and $Nu = 0.145Ra^{0.29}$ (Tanaka & Miyata 1980), which yield estimates $Nu \simeq 56$ and $Nu \simeq 59$, respectively, at $Ra = 10^9$.

Ahlers & Xu (2001) studied convection using four organic fluids with Prandtl numbers in the range $4 \leqslant Pr \leqslant 34$ for Rayleigh numbers up to $10^{11}$ using aspect ratio 0.5 and 1.0 cells. They do not report a scaling law for their data, but by reading from their figures it can be estimated that the Nusselt number decreases from $Nu \simeq 65.5$ at $Pr \simeq 4$ to $Nu \simeq 64.5$ at $Pr \simeq 34$ for the aspect ratio 0.5 cell. Results are a few per cent lower for the unit-aspect-ratio cell. These results use a model to correct the measured heat current at the sidewalls, and they note that if this model were applied to the helium convection data of Niemela *et al.* (2000), the result would be to lower the Nusselt number from $Nu \simeq 75$ to $Nu \simeq 60$ at $Ra = 10^9$. However, in figure 2 we chose to present the helium data as published by the original authors, without corrections suggested by subsequent authors.

Another experiment using a variety of liquids to study convection over a range of Prandtl number in the same unit-aspect-ratio cell has been conducted by Xia *et al.* (2002). They use nine working fluids covering the range $4.3 \leqslant Pr \leqslant 1352$. The Rayleigh number range is $2 \times 10^7 \leqslant Ra \leqslant 3 \times 10^{10}$, although no single fluid spans this entire range. They do not report results for individual fluids, but instead summarize their data with the approximate relationship $Nu = 0.14Pr^{-0.03}Ra^{0.297}$. This scaling is used to produce the $Nu(Pr)$ curve shown in figure 2. At $Pr = 4$, their results are very similar to the (corrected) results of Ahlers & Xu (2001), but the decrease of $Nu$ as $Pr$ increases is more pronounced in their work.

The scaling of $Nu$ with $Ra$ at $Pr \simeq 2750$ has been explored using electrochemical convection by Goldstein, Chiang & See (1990). They report $Nu \simeq 0.0659Ra^{1/3}$ over the range $3 \times 10^9 \leqslant Ra \leqslant 5 \times 10^{12}$ in a large-aspect-ratio cell. Extrapolating this scaling to $Ra = 10^9$ gives $Nu \simeq 66$, which is 25% larger than an extrapolation of the results of Xia *et al.* (2002) would give for the same $Ra$ and $Pr$.

Comparing ODT and experimental data in figure 2, we see that there is good agreement with the mercury data, since the ODT parameter $C$ was chosen to achieve this. The ODT results for $ZC^2 = 823$ and $ZC^2 = 10^4$ both fall near the range of observed $Nu$ values for helium. The $ZC^2 = 10^5$ data underpredict $Nu$ for He but match the water data well. The $ZC^2 = 10^4$ and $ZC^2 = 10^5$ data bracket the results of Ahlers & Xu (2001) and Xia *et al.* (2002). Simulation and experiment both exhibit a trend of decreasing $Nu$ as $Pr$ increases, but the trend is slightly stronger in the ODT data than in the experiments. The $ZC^2 = 823$ data best match the electrochemical convection result (the value $ZC^2 = 823$ was selected to match that experiment), which

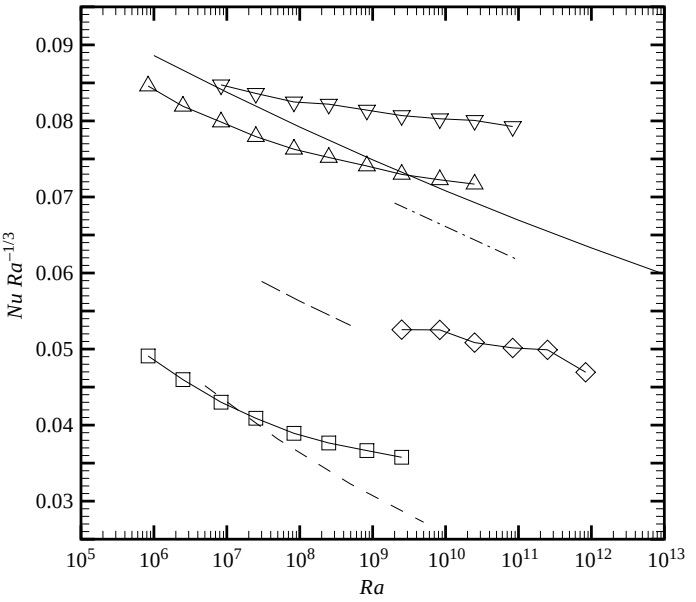


FIGURE 3. $Nu$ as a function of $Ra$ for $ZC^2 = 10^4$ and $C^2 = 1200$. Symbols are ODT simulation results for □, $Pr = 0.025$; △, 0.7; ▽, 4; ◇, 1352. Lines are reported fits to experimental data for $Pr = 0.025$ from Cioni *et al.* (1997) (dashed line), $Pr = 0.7$ from Niemela *et al.* (2000) (solid line), $Pr = 4$ from Ahlers & Xu (2002) without sidewall heat loss correction (dot-dashed line), and $Pr = 1352$ from Xia *et al.* (2002) (long-dashed line).

indicates a much larger value of $Nu$ than would be expected based on the results of Xia *et al.* (2002). No attempt to resolve this discrepancy is made here.

Figures 3 and 4 illustrate the dependence of $Nu$ on $Ra$ in the ODT model for $ZC^2 = 10^4$ and $10^5$, respectively, and several different values of $Pr$. Experimental results shown for comparison were selected to be representative of a wide range of $Pr$ values; all possible experiments cannot be shown without loss of clarity. The vertical axis shows $NuRa^{-1/3}$, so that horizontal lines would indicate purely classical scaling. All ODT data exhibit approximate scaling exponents in the range 0.27 to 0.33, depending on $Pr$ and $Ra$. Plotting $NuRa^{-1/3}$ also magnifies differences between ODT and experimental results, since actual values of $Nu$ vary by more than two orders of magnitude while values of $NuRa^{-1/3}$ vary only by a factor of about two.

For $ZC^2 = 10^4$ (figure 3), the ODT data agree very well with the mercury convection data of Cioni *et al.* (1997), with the largest discrepancy being only about 15%. The $Pr = 0.7$ ODT results match the helium data of Niemela *et al.* (2000) to within 5%, and the high-Prandtl-number case plausibly matches the data of Xia *et al.* (2002), although the range of Rayleigh numbers do not overlap. However, the ODT $Nu$ values for $Pr = 4$ consistently exceed those of Ahlers & Xu (2002) by about 25%. The experimental data shown in figure 3 neglect the sidewall heat-loss model proposed by Ahlers & Xu (2002), which would lower the experimental $Nu$ values even further.

In figure 4, ODT data for $ZC^2 = 10^5$ are compared to data from the same experiments as in figure 3. However, the data from Ahlers & Xu (2002) is shown with correction from the sidewall heat-loss model, and the data from Niemela *et al.* (2000) is also shifted downward according to this correction as suggested by Ahlers & Xu (2002). This allows a consistent comparison, and is not meant to imply that either choice is necessarily correct. For this larger value of $ZC^2$, the model data at

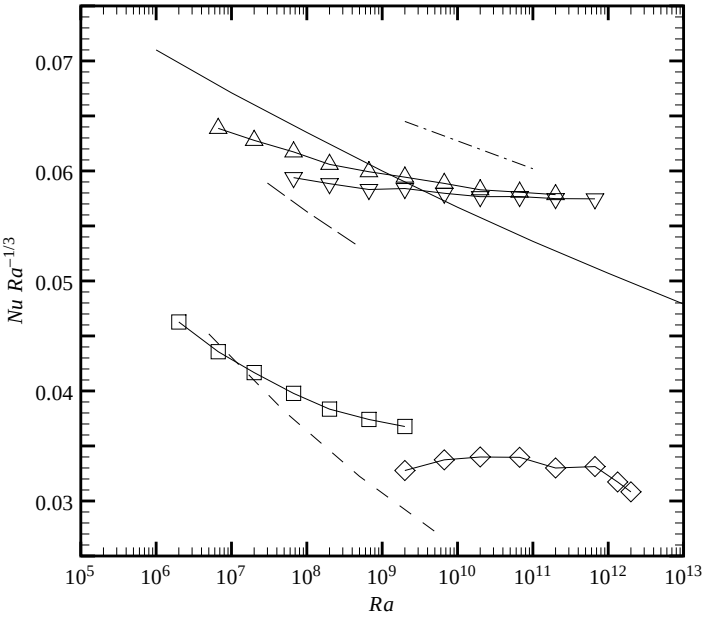


FIGURE 4. *Nu* as a function of *Ra* for $ZC^2 = 10^5$ and $C^2 = 1500$. Symbols are ODT simulation results for □, $Pr = 0.025$; △, 0.7; ▽, 4; ◇, 1352. Lines are reported fits to experimental data for $Pr = 0.025$ from Cioni *et al.* (1997) (dashed line), $Pr = 0.7$ from Niemela *et al.* (2000) as corrected for sidewall heat loss by Ahlers & Xu (2002) (solid line), $Pr = 4$ from Ahlers & Xu (2002) with sidewall heat loss correction (dot-dashed line), and $Pr = 1352$ from Xia *et al.* (2002) (long-dashed line).

low Prandtl number exhibit a larger scaling exponent of *Nu* with *Ra* than is seen for $ZC^2 = 10^4$ or in the data of Cioni *et al.* (1997). These results are closer to the experimental data of Takeshita *et al.* (1996), however (not shown). The data for $Pr = 0.7$ and $Pr = 4$ are also closer to the classical scaling of 1/3, but differ from the experimental data by less than 10% despite the difference in scaling exponents. The $Pr = 1352$ data exhibit approximately classical scaling and are lower than the extrapolated results of Xia *et al.* (2002) by about 50%. Overall, it is seen that increasing $ZC^2$, in addition to shifting the peak of the $Nu(Pr)$ curve in figure 2, also results in $Nu(Ra)$ scaling which is closer to the classical value 1/3 over the range of *Ra* simulated.

Figures 2 to 4 demonstrate that ODT reproduces the qualitative trends observed in convection cell experiments. Quantitative agreement depends on the interpretation of sidewall heat loss and the effects of aspect ratio, which are not represented in the model. Hence, it is not possible to determine if there exists a particular choice of parameters $C$ and $ZC^2$ for which the model would correctly reproduce $Nu(Ra, Pr)$ in an infinite-aspect-ratio system. However, the values of *Nu* produced by the model are adequate for study of the core fluctuations, which requires only that the heat transfer rate approximate the physical value for a given choice of the Rayleigh and Prandtl numbers.

### 4.2. *Core temperature fluctuations*

In the ODT simulations, a significant temperature gradient is observed in the core of the convection cell. The presence of a temperature gradient (on average) in experimental cells has not been confirmed or ruled out (to our knowledge). Its appearance in the model simulations is explained using a simple flux-balance argument.

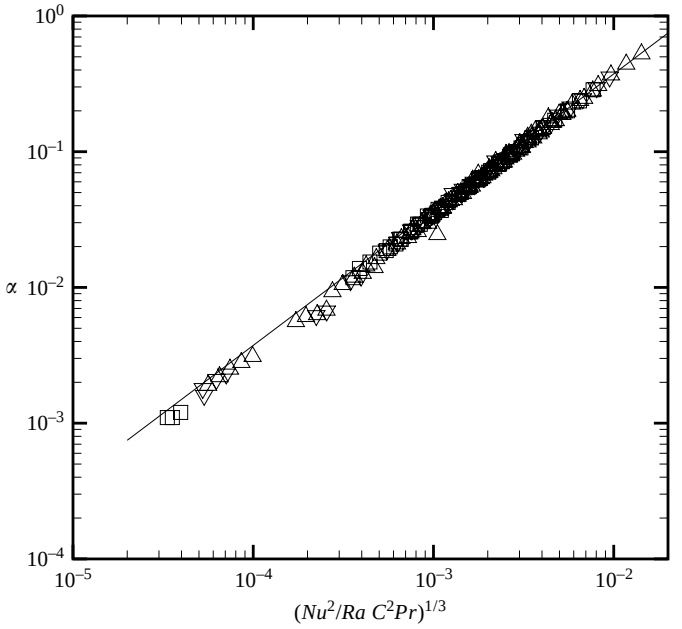


FIGURE 5. Magnitude of the core temperature gradient. Symbols are ODT simulation results for three different values of $ZC^2$: $\triangle$, $ZC^2 = 823$; $\nabla$, $10^4$; $\square$, $10^5$. The line is $\alpha = 37.4\ (Nu^2/RaC^2Pr)^{1/3}$.

Assuming a constant temperature gradient across the core region, the average temperature $\langle \delta T(y) \rangle$ is expressed in the form

$$\frac{\langle \delta T(y) \rangle}{\Delta T} = \tfrac{1}{2} + \alpha \left( \frac{y}{\Lambda} - \frac{1}{2} \right), \tag{4.1}$$

which defines the dimensionless gradient $\alpha$ as the ratio of the average gradient in the core to the mean gradient $\Delta T/\Lambda$. The core gradient can be quite substantial, often exceeding $\alpha \sim 0.1$ for low values of $Ra$ and $Pr$.

The magnitude of the core temperature gradient $\alpha$ is estimated by considering the transport properties of the interior. The heat flux $F$ through the core is estimated for eddies comparable in size to the cell height $\Lambda$ (these largest eddies dominate transport) as

$$F \sim \frac{\Lambda}{\tau_\Lambda} \alpha \Delta T, \tag{4.2}$$

where $\tau_\Lambda$ is the eddy turnover time and $\alpha \Delta T$ is the typical temperature variation across the core of the cell. Assuming this temperature difference is the driving force behind this transport, the typical turnover time is $\tau_\Lambda \sim (gC^2 \alpha \beta \Delta T/\Lambda \rho_0)^{-1/2}$. The flux is then

$$F \sim \frac{\kappa \Delta T}{\Lambda} \alpha^{3/2} (RaC^2Pr)^{1/2}. \tag{4.3}$$

This flux must balance the flux at the wall, given by $F \sim Nu\, \kappa \Delta T/\Lambda$. Enforcing this balance yields

$$\alpha \sim \left( \frac{Nu^2}{RaC^2Pr} \right)^{1/3}. \tag{4.4}$$

Figure 5 demonstrates this correlation using values of $\alpha$ determined by fitting the average temperature profile in each ODT simulation to a line in the middle 3/4 of the

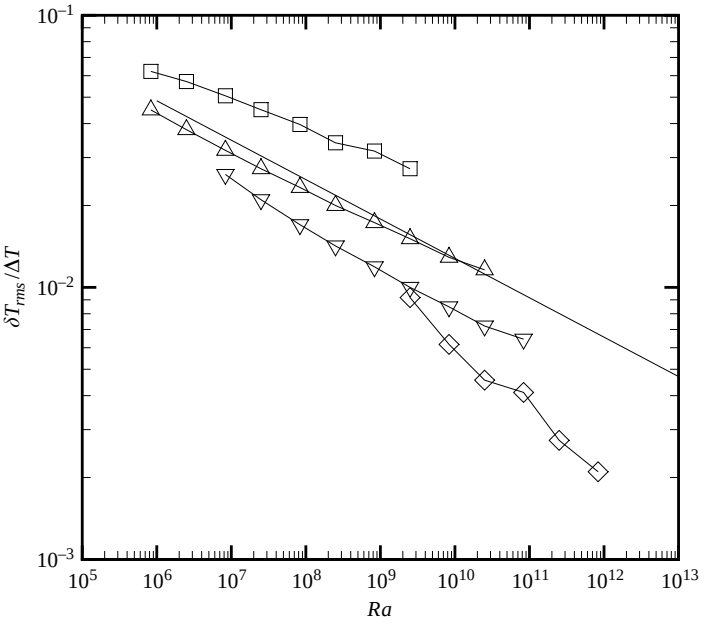


FIGURE 6. Magnitude of temperature fluctuations in the interior. Symbols are ODT simulation results for $ZC^2 = 10^4$ at □, $Pr = 0.025$; △, 0.7; ▽, 4; ◇, 1352; the solid line is $\delta T_{rms}/\Delta T = 0.37 Ra^{-0.145}$, a reported fit to $Pr = 0.7$ experimental data by Niemela *et al.* (2000).

cell. The correlation is independent of the value of $Z$, which is expected since (4.4) is based on large-scale transport. The value of $C$ does matter, since this parameter sets the large-eddy turnover rate and, hence, the overall heat transfer.

The larger values of the core temperature gradient ($\alpha \geqslant 0.1$) shown in figure 5 occur at low $Pr$. The high molecular diffusivity in these cases generates a large flux at the wall, which must be balanced in the core by turbulent transport along a large temperature gradient. At low $Pr$, the large value of $\alpha$ probably influences the dynamics of the thermal boundary layers and consequently plays a role in the observed non-classical scaling of $Nu$ with $Ra$.

Figure 6 shows the magnitude of the temperature fluctuations observed in the core of the cell for the representative cases presented in figures 3 and 4. In this study, the fluctuations $\delta T_{rms}$ are defined as the root-mean-square (r.m.s.) deviations from the average temperature profile, and the 'core' is defined as the middle 1/4 of the cell. This definition eliminates the spatial variability due to the mean temperature gradient, making the data comparable to experimental data taken at a single point. The experimentally observed temperature fluctuation magnitude for helium ($Pr = 0.7$) is also shown (Niemela *et al.* 2000), and the agreement with the ODT data for $ZC^2 = 10^4$ is excellent (errors less than 10%) at this Prandtl number. This value of $ZC^2$ also gave the best agreement with the corresponding Nusselt-number data.

The $Pr$ dependence of ODT results for $\delta T_{rms}$, which is evident in figure 6, is further illustrated in figure 7. For any given $ZC^2$, there is a minimum value of $\delta T_{rms}$ which occurs at $Pr \sim 200$ for $ZC^2 = 823$, but shifts to $Pr \sim 50$ for $ZC^2 = 10^4$ and $Pr \sim 20$ for $ZC^2 = 10^5$. Figure 7 also shows that $\delta T_{rms}$ depends only weakly on $ZC^2$ at low Prandtl number. For comparison, experimental values for helium (Niemela *et al.* 2000) and water solutions at several Prandtl numbers at a larger $Ra$ value (Daya &

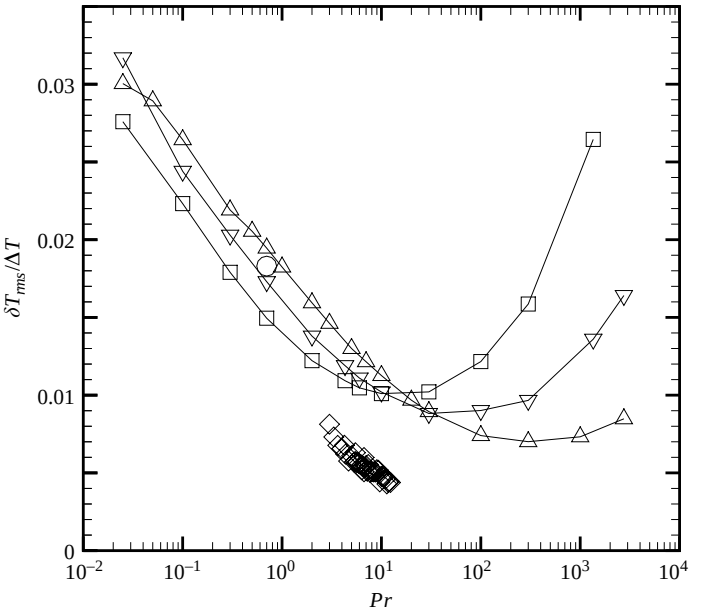


FIGURE 7. Magnitude of temperature fluctuations in the interior as a function of $Pr$ at $Ra = 10^9$. △, ODT data for $ZC^2 = 823$; ▽, $ZC^2 = 10^4$; □, $ZC^2 = 10^5$. ○, experimental data for helium (He) at the same Rayleigh number (Niemela *et al.* 2000); ◇, experimental data for water solutions at a number of $Pr$ values for $Ra = 2 \times 10^9$ (Daya & Ecke 2002).

Ecke 2002) are also shown. Again, the helium data compare favourably to the ODT simulations, and the water solutions exhibit the same trend with $Pr$, although the absolute magnitude is smaller by a factor of approximately two.

Estimation of the $Ra$ scaling of the ODT core temperature fluctuations $\delta T_{rms}$ for many values of $Pr$ indicated that the scaling exponent exhibits a strong dependence on the Prandtl number. (Simulations at $Ra = 10^8$ and $Ra = 10^9$ were used to calculate the scaling exponents.) At the smallest Prandtl number simulated ($Pr = 0.025$), the scaling exponent is approximately $-0.11$. It slowly becomes more negative until $Pr$ reaches the value corresponding to the minimum of $\delta T_{rms}(Pr)$ seen in figure 7 (a value which varies slightly with $ZC^2$), and then decreases rapidly to $-0.3$ for $Pr = 1352$. These scaling exponents show only weak dependence on the value of $ZC^2$. For $Pr = 0.7$, the ODT value of $-0.13$ compares favourably to the experimental values of $-0.145$ (Niemela *et al.* 2000) and $-0.147 \pm 0.005$ (Castaing *et al.* 1989). For $Pr = 5.5$, Daya & Ecke (2001) report an exponent of $-0.10 \pm 0.02$, which is less negative than the model exponent of $-0.15$. Daya & Ecke (2002) also report that the scaling exponent becomes more negative as $Pr$ increases, reaching $-0.18$ for $Pr = 10$ (compared to $-0.17$ for ODT at $Pr = 10$). Thus, the ODT exponents follow the trend found by Daya & Ecke (2002), although the dependence on $Pr$ is somewhat weaker.

A simple picture of the temperature fluctuations yields a crude estimate of the $Ra$ and $Pr$ dependence of $\delta T_{rms}$. In this view, there are two distinct sources of core temperature fluctuations. One is the mixing of the core temperature gradient by eddies, whose contribution to the mean-square core temperature fluctuations is labelled $\delta T^2_{core}$. The other is the transport of fluid elements from the thermal boundary layers directly to the core region by plumes which reach the core with minimal diffusive mixing; this contribution is labelled $\delta T^2_{BL}$. Assuming that these two contributions are statistically

independent, the total r.m.s. temperature fluctuation is given by (see Appendix)

$$\delta T_{rms}^2 = \delta T_{core}^2 + \delta T_{BL}^2. \tag{4.5}$$

The contribution $\delta T_{core}^2$ due to the core fluctuations is proportional to $(\alpha \Delta T)^2$ (where $\alpha$ is given by (4.4)), since this is the total temperature variation across the core region. Estimating the boundary-layer contribution requires an understanding of the frequency with which large eddies (the ODT equivalent of plume motion) transport a substantial fraction of the boundary layer directly into the core region. Each eddy transports a 'blob' of fluid whose width scales as $\Lambda/Nu$ (the boundary-layer thickness) with a temperature fluctuation of order $\Delta T$. These blobs appear in the core region with some frequency $\tau_b^{-1}$ and survive in the core for some lifetime $\tau_l \ll \tau_b$. Their total contribution to the temperature fluctuations is

$$\delta T_{BL}^2 \sim \Delta T^2 Nu^{-1}(\tau_l/\tau_b), \tag{4.6}$$

based on a space–time average over many blobs. The typical frequency $\tau_b^{-1}$ is estimated from the energy released when a blob with mass of the order of $\Lambda \beta \Delta T/Nu$ is transported a distance of order $\Lambda$:

$$\tau_b^{-1} \sim \sqrt{\frac{g\beta\Delta T}{Nu\rho_0\Lambda}}. \tag{4.7}$$

The lifetime $\tau_l$ of the blob in the turbulent core is more difficult to determine, but a plausible estimate is to use the turnover time of the smallest (Kolmogorov-scale) eddies. This assumes that the typical blob which breaks off from the thermal boundary layer is smaller than the Kolmogorov scale, an assumption which has been verified in ODT for larger Prandtl numbers ($Pr \geqslant 1$). Therefore, the smallest eddies are the relevant ones for blob break-up and dissipation. The blob lifetime therefore scales as $\tau_l \sim (\Lambda^2/\nu) Re^{-3/2}$, where $Re$ is the Reynolds number based on the velocity scale in the core of the cell where the blob is broken up (not the 'wind' velocity scale). It is shown in § 4.3 that $Re$ in the core of the cell scales as $Re^3 \sim RaNuPr^{-2}$. Combining these time scales yields

$$\delta T_{BL}^2 \sim \Delta T^2 \frac{Pr^{1/2}}{Nu^2} \tag{4.8}$$

for the boundary-layer contribution, and an overall expression for $\delta T_{rms}$ of

$$\left(\frac{\delta T_{rms}}{\Delta T}\right)^2 = A\left(\frac{Nu^2}{RaC^2Pr}\right)^{2/3} + B\frac{Pr^{1/2}}{Nu^2}, \tag{4.9}$$

where $A$ and $B$ are constants. In the limit $Pr \to 0$, the core gradient is large and the boundary-layer contribution to $\delta T_{rms}$ is negligible. This yields the classical result $\delta T_{rms} \sim \Delta T(RaPr)^{-1/9}$ if $Nu \sim (RaPr)^{1/3}$ (Siggia 1994). This is comparable to the observed ODT Rayleigh number scaling exponent of $-0.11$ in the $Pr = 0.025$ case. In the other limit, $Pr \to \infty$, the core gradient vanishes and the boundary-layer contribution increases until it dominates the fluctuations. In this case, $\delta T_{rms} \sim \Delta T Ra^{-1/3}$ (assuming $Nu \sim Ra^{1/3}$), which is consistent with the value $-0.3$ inferred from the $Pr = 1352$ ODT data. Intermediate values of $Pr$ yield exponents that lie between these limits, since the sum of two scaling functions with distinct exponents mimics a scaling function with an intermediate exponent value. The different scalings with $Ra$ observed at different values of $Pr$ in figure 6 may therefore be attributed to changes in the relative contributions of the two terms in (4.9). The fluctuation

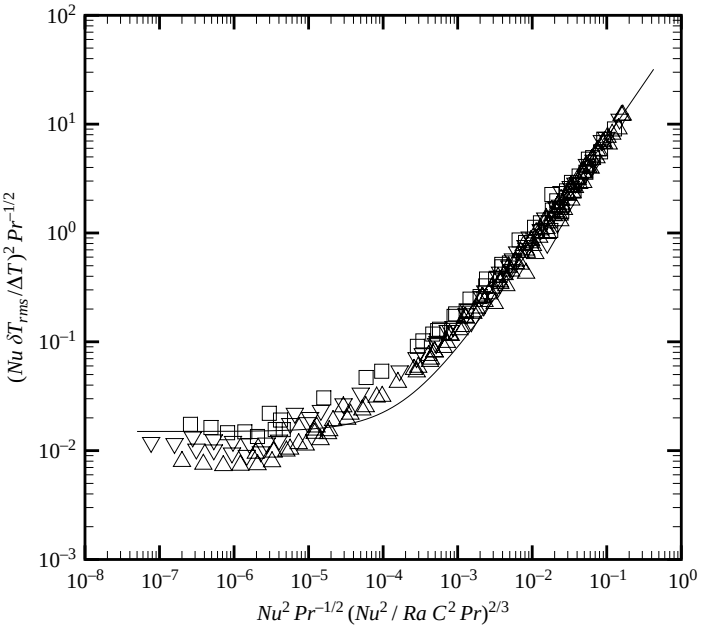


FIGURE 8. Scaling of the temperature fluctuations, as suggested by a simple model with two sources of fluctuations. △, ODT simulation data for $ZC^2 = 823$; ▽, $ZC^2 = 10^4$; □, $ZC^2 = 10^5$. The line is a fit of (4.9) with $A = 75$ and $B = 0.015$.

magnitude estimate of (4.9) also produces a minimum at a $Pr$ value where both terms contribute substantially to the total, which is consistent with the ODT data shown in figure 7. At small $Pr$, the first term dominates and $\delta T_{rms}$ is a decreasing function of $Pr$, as seen in figure 7. At large $Pr$, the second term in (4.9) increases with $Pr$ since $Nu$ decreases with $Pr$ for large values of $Pr$ (see figure 2). This causes the increase in $\delta T_{rms}$ with $Pr$ as $Pr \to \infty$, as seen in figure 7. For a fixed value of $Pr$, the core term always dominates in the limit $Ra \to \infty$ (assuming the $Nu(Ra)$ scaling exponent exceeds 1/5).

Figure 8 illustrates the scaling suggested by (4.9) for all of our ODT simulation data. The results are shown on a logarithmic scale since the normalized temperature fluctuations vary over several orders of magnitude. This illustrates the parameter regime where the core contribution dominates (upper right-hand portion of figure 8) as well as the regime where the boundary layer dominates and $((\delta T_{rms}/\Delta T)Nu)^2 Pr^{-1/2}$ is approximately constant (lower left-hand portion of figure 8). The line shows a fit of (4.9) to the data. However, while the same value of $A$ matches all three values of $ZC^2$, it is clear from figure 8 that slightly different values of $B$ would best match the data for each value of $ZC^2$. Hence, although the core contribution to $\delta T_{rms}$ appears to be independent of $ZC^2$, the boundary-layer contribution apparently increases as $ZC^2$ increases. Figure 8 shows that, although (4.9) gives good agreement with the ODT data in the limiting cases where either the core or boundary-layer contributions dominate, it is imperfect in the portion of parameter space where both are significant. The assumption of statistical independence of the two contributions is probably at least partially responsible for this error. However, even at its worst, the estimate of (4.9) is within 40% of the ODT results, which is good considering that $\delta T_{rms}$ varies by over two orders of magnitude.

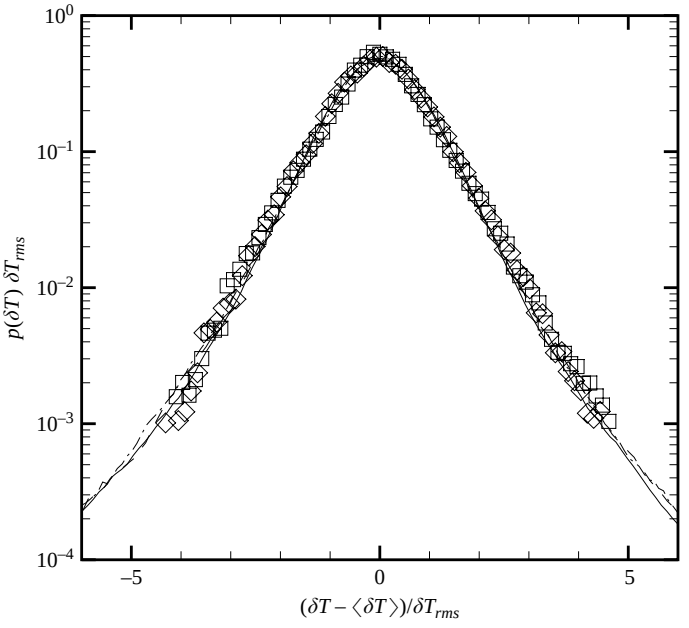


FIGURE 9. Rescaled probability density $p$ of a temperature fluctuation $\delta T$ (lines) for $Pr = 5.5$, $Ra = 2 \times 10^9$. The three lines correspond to ODT results for the three values of $ZC^2$: dash-dotted for $ZC^2 = 823$, dashed for $ZC^2 = 10^4$, and solid for $ZC^2 = 10^5$. The shape is independent of $ZC^2$. Here, $\langle \delta T \rangle = 0.5 \Delta T$ and $\delta T_{rms}^2$ is the variance of the p.d.f. For comparison, experimental data in two distinct cell geometries (□, cylindrical geometry; ◇, rectangular geometry) with the same $Ra$ and $Pr$ are also shown (Daya & Ecke 2001).

It is worth recognizing that the separation of the temperature fluctuations into two distinct sources is somewhat artificial, since it is obvious that all fluctuations must ultimately originate in the thermal boundary layers. It is perhaps better to think of the contribution of the core temperature gradient as representing the effects of fluid elements which interact significantly with their environment while transiting from the boundary layer to the cell centre (producing the average temperature gradient), while the explicit boundary-layer contribution to (4.9) represents the effects of plumes which reach the cell centre with minimal interaction. In ODT, the difference between these two mechanisms arises because fluid elements may transit from boundary layer to cell centre either indirectly, as a result of a large number of eddy mappings (allowing some equilibration with the environment along the way) or directly as a result of only one or two mappings (allowing little time for equilibration).

To study the statistics of the temperature fluctuations in the core of the cell, we collected temperature values in narrow spatial intervals 1/64 of the cell height $\Lambda$ in length. Figure 9 shows the probability density function (p.d.f.) of temperature values observed at the centre of the cell, normalized by $\delta T_{rms}$ (the square root of the p.d.f. variance), for $Pr = 5.5$ and $Ra = 2 \times 10^9$. Results for all three values of $ZC^2$ are shown. Generally, ODT p.d.f. shapes do not appear to depend on the value of $ZC^2$ except when extreme fluctuations (ten or more standard deviations) are considered. The p.d.f. shape is approximately exponential out to at least 6 standard deviations. Experimental data (Daya & Ecke 2001) for the same $Ra$ and $Pr$ are also shown in figure 9, and the p.d.f. shapes are nearly identical. These data were collected in two different geometries – a cylindrical cell and a square cell – yet the p.d.f. shapes match

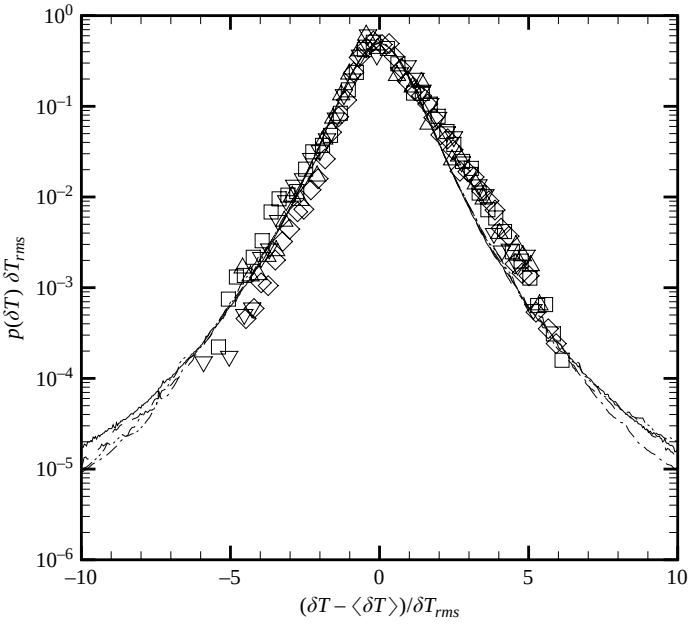


FIGURE 10. Rescaled probability density $p$ of a temperature fluctuation $\delta T$ for $Pr = 0.7$ and $ZC^2 = 10^5$, using the same normalization as in figure 9. ODT results (lines) for four distinct $Ra$ values ($Ra = 2 \times 10^7$, solid line; $2 \times 10^8$, dashed line; $2 \times 10^9$, dash-dotted line; and $2 \times 10^{10}$, dash-dot-dotted line) are shown, but the shapes are indistinguishable to 6 standard deviations. For comparison, experimental data (symbols) for helium convection (Castaing *et al.* 1989) is also shown for four $Ra$ values between $10^8$ and $10^{12}$.

each other and ODT. However, the values of $\delta T_{rms}$ used to normalize the p.d.f.s are different in all three cases. Hence, it seems that, while the value of $\delta T_{rms}$ may depend strongly on geometry, the p.d.f. shape is more universal and is correctly generated by ODT. This suggests that the physical mechanism which detemines the shape is relatively simple and accessible to the model.

It was recognized in the helium convection experiments of Castaing *et al.* (1989) that the universal shape of the p.d.f. when normalized by $\delta T_{rms}$ applies over a wide range of Rayleigh numbers. Figure 10 illustrates this collapse for $Pr = 0.7$ for four values of $Ra$ spanning three orders of magnitude. The results for $ZC^2 = 10^5$ are shown here and in subsequent figures because more statistics were collected for those simulations than for smaller values of $ZC^2$, but, as previously noted (see figure 9), the shape does not depend on $ZC^2$ over the range of fluctuations shown. Again, the simulation p.d.f.s are approximated well by an exponential form within six standard deviations of zero. The experimental data of Castaing *et al.* (1989) are also shown in figure 10 for comparison. To facilitate a direct comparison, histogram data from their paper were digitized and normalized to produce the approximate p.d.f.s shown in figure 10. While there is excellent agreement for negative fluctuations, the experimental p.d.f. exhibits an asymmetry which the (inherently symmetric) model does not have.

The collapse of the p.d.f.s must ultimately fail at large deviations because $|\delta T - \langle \delta T \rangle|$ is bounded by $0.5\Delta T$ owing to the finite cell size. This breakdown is observed in ODT as a long non-exponential tail in the p.d.f. followed by the truncation of the p.d.f. at $|\delta T - \langle \delta T \rangle| = 0.5\Delta T$. The separation of the p.d.f.s is seen in figure 10 beginning at approximately 8 standard deviations.

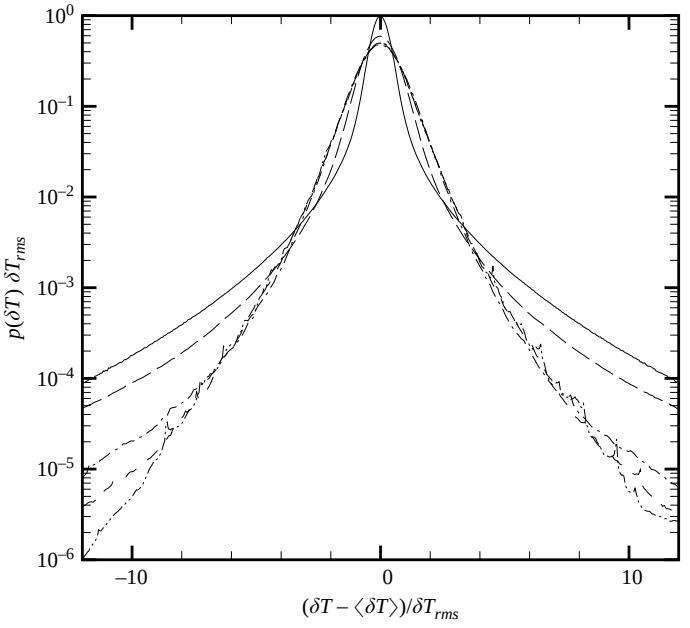


FIGURE 11. Rescaled probability density $p$ in ODT of a temperature fluctuation $\delta T$ for $Ra = 2 \times 10^9$, $ZC^2 = 10^5$, and five $Pr$ values: 0.1, dash-dot-dotted line; 0.7, dashed line; 4, dash-dotted line; 100, long-dashed line; and 1352, solid line. The rescaled probability density of large fluctuations increases with $Pr$.

The collapse of the p.d.f. cores illustrated in figures 9 and 10 is tested for different $Pr$ values (at fixed $Ra$) in figure 11. Although the low-$Pr$ case is more noisy than the others, the $Pr = 0.1$, $Pr = 0.7$ and $Pr = 4$ p.d.f.s appear to overlap within five standard deviations, of the average temperature value. At very large deviations, the p.d.f.s progressively diverge from each other, with the probability of very large deviations increasing with $Pr$. However, the $Pr = 100$ and $Pr = 1352$ simulations exhibit sharper p.d.f. cores and do not match the others. Hence, it appears that the collapse of the p.d.f.s proposed by Castaing *et al.* (1989) does not apply to high-$Pr$ data in the ODT model.

The fact that the rescaled p.d.f. shape appears to be independent of $Ra$ and $Pr$ for $Pr < 100$ indicates that the same mechanism is operative over this wide range of parameter values. Based on the previous analysis of the magnitude of the temperature fluctuations which led to (4.9), this shape is apparently the result of the transport of fluid elements from boundary layer to core via the 'indirect transport' (or core gradient) process in which a fluid element interacts significantly with its environment while passing from boundary layer to cell centre. This is inferred because this contribution dominates the estimate of $\delta T_{rms}$ at low $Pr$ values in (4.9). The transition to a different p.d.f. shape at larger $Pr$ values is seen in simulations in which the 'direct transport' mechanism, in which plumes move from boundary layer to cell centre without much equilibration with their environment during transit, becomes the dominant contribution to $\delta T_{rms}$ in (4.9). Hence, the two distinct p.d.f. shapes are apparently indicative of the two distinct contributions to the magnitude of the density fluctuations $\delta T_{rms}$. This analysis suggests that observations of the p.d.f.

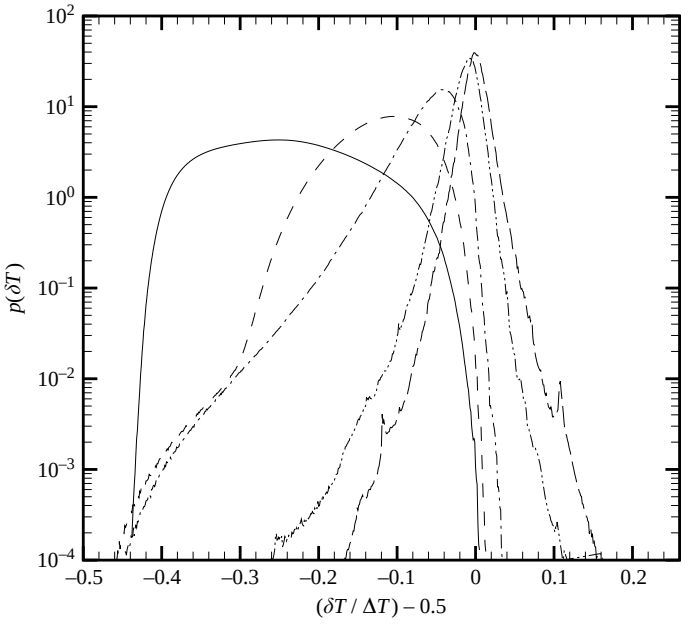


FIGURE 12. Probability density $p$ in ODT of a temperature fluctuation $\delta T$ for $Ra = 2 \times 10^9$, $Pr = 0.7$, and $ZC^2 = 10^5$, at 5 distinct vertical locations: $0.004\Lambda$, solid line; $0.0078\Lambda$, dashed line; $0.031\Lambda$, dash-dotted line; $0.25\Lambda$, dash-dot-dotted line; and $0.5\Lambda$, long-dashed line. The thermal boundary-layer thickness in this case is approximately $0.008\Lambda$.

in high-$Pr$ convection experiments, such as those of Xia *et al.* (2002), might reveal a different shape from that which has been previously seen experimentally.

The shape of the p.d.f. of temperature values depends strongly on the vertical location within the convection cell. A series of p.d.f.s at different heights in the lower half of the cell is shown in figure 12. The data are taken from the $Ra = 2 \times 10^9$, $Pr = 0.7$ simulation. The mean value of each p.d.f. increases with the distance from the lower plate, and the shape changes as well. The lowest location shown lies within the thermal boundary layer (the boundary-layer thickness is about $0.008\Lambda$ in this case), and the second lowest location is just above the boundary layer. The others are within the convective core of the cell.

Figure 13 shows the p.d.f.s of temperature values at the off-centre location $y = 0.25\Lambda$ for the same $Pr = 0.7$ simulations as figure 10. Again, the results are normalized by the r.m.s. value of the temperature fluctuations. Since the location lies closer to the bottom plate (where $\delta T = 0$) than to the top (where $\delta T = \Delta T$), it is not surprising that negative values of $\delta T - \langle \delta T \rangle$ are much more frequent than positive values. Long tails which vary slightly with $Ra$ are evident on the left-hand side of the p.d.f., with larger $Ra$ giving a higher probability of large negative deviations. The right-hand side of the p.d.f. falls off much more steeply than the p.d.f. in the cell centre (see figure 10). Apparently, the increased distance from the upper boundary layer (compared to the cell centre p.d.f.) results in a faster decrease in the p.d.f. To our knowledge, there are no published experimental data on off-centre temperature fluctuation p.d.f.s for comparison with the model data. Off-centre p.d.f.s at $y = 0.75\Lambda$ (not shown) are approximately a mirror image of figure 12, as expected.

Off-centre p.d.f.s (at $y = 0.25\Lambda$) for five different Prandtl numbers are shown in figure 14. As in figure 11, the large-$Pr$ and small-$Pr$ p.d.f.s exhibit two distinct shapes

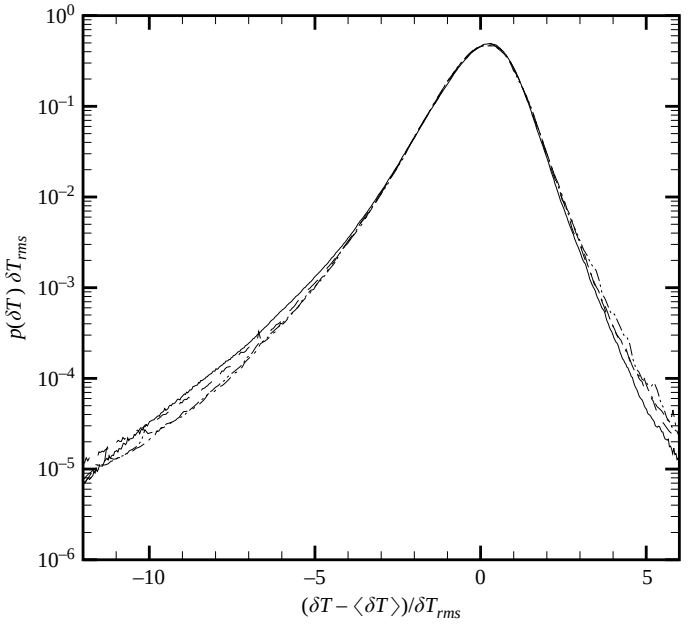


FIGURE 13. Rescaled off-centre probability density $p$ in ODT of a temperature fluctuation $\delta T$ for $Pr = 0.7$, $ZC^2 = 10^5$, and the same $Ra$ values shown in figure 10 ($Ra = 2 \times 10^7$, solid line; $2 \times 10^8$, dashed line; $2 \times 10^9$, dash-dotted line; and $2 \times 10^{10}$, dash-dot-dot line). The position is $y = \Lambda/4$.

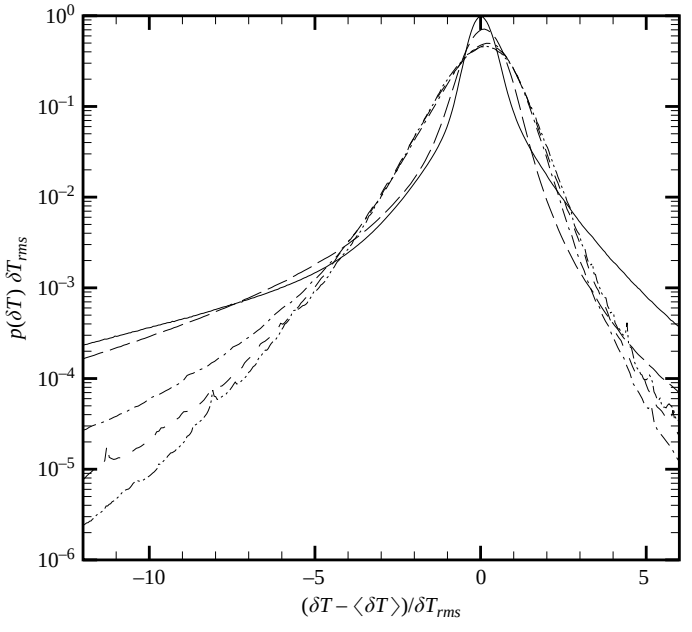


FIGURE 14. Rescaled off-centre probability density $p$ in ODT of a temperature fluctuation $\delta T$ for $Ra = 2 \times 10^9$, $ZC^2 = 10^5$, and five values of $Pr$: 0.1, dash-dot-dotted line; 0.7, dashed line; 4, dash-dotted line; 100, long-dashed line; and 1352, solid line. The rescaled probability density of a large negative fluctuation increases with $Pr$, as in figure 11.

at small standard deviations. Also, there is a higher probability of large-deviation events at higher $Pr$. The asymmetry due to the proximity to the lower cell boundary is again evident.

### 4.3. *Core velocity fluctuations*

The magnitude of the ODT velocity fluctuations in the core of the cell can be estimated using energy conservation (2.12) and the characteristics of the turbulent cascade, which the model mimics by design in the absence of a temperature gradient. Because the temperature is nearly constant in the core of the cell, the turbulent cascade operates with little interference in most of the cell. It is therefore plausible to estimate the energy dissipation based on the cell size $\Lambda$ and the typical velocity scale $U$ in the cell core. The energy input to the cascade at the large scale is $U^3/\Lambda$; balancing this against the dissipation (assuming a steady cascade) implies

$$\frac{U^3}{\Lambda} \sim \nu \langle (\partial_y v)^2 \rangle. \tag{4.10}$$

The dimensionless energy dissipation $\epsilon$ is therefore

$$\epsilon \equiv \frac{\Lambda^3}{\nu^2} \int \langle (\partial_y v)^2 \rangle \mathrm{d}y \sim \frac{U^3 \Lambda^3}{\nu^3} \equiv Re^3, \tag{4.11}$$

where $Re \equiv U\Lambda/\nu$ is the Reynolds number. To establish a quantitative relationship, the velocity scale $U$ is defined as $U \equiv \sqrt{\langle v^2 \rangle} \equiv v_{rms}$, where the average is taken over the middle 1/4 of the cell (to avoid wall effects) and over the time history of the simulation. Hence, the ODT $Re$ is a measure of the r.m.s. velocity fluctuations in the core. Using this definition, the proportionality between $Re^3$ and energy dissipation $\epsilon$ is obeyed in the ODT simulations to within a few per cent.

A corollary of this scaling, due to the energy conservation equation (2.12), is a relationship between the magnitude of the velocity fluctuations $Re$ and the heat transfer $Nu$:

$$RePr = 1.4C^{-1/3}(RaPr(Nu-1))^{1/3}, \tag{4.12}$$

with the constant of proportionality, $1.4C^{-1/3}$, determined by fitting the simulation data for all values of $ZC^2$. Although superficially similar to one of the relationships used by Grossmann & Lohse (2000), (4.12), in fact, differs from the previous result because $Re$ is defined in terms of the core velocity fluctuations, whereas in Grossmann & Lohse (2000) it is defined in terms of the large scale 'wind' velocity. This relation is demonstrated for the ODT simulations in figure 15. Hence, by combining energy conservation with the assumption of a turbulent cascade, a non-trivial relationship (4.12) for the magnitude of the ODT velocity fluctuations has been obtained, in agreement with the simulation data.

A few experiments have attempted to measure velocity fluctuations and estimate $Re$ in the convection cell. Using published scaling estimates for $Re$ and $Nu$, the experimental results for different Prandtl numbers are given approximately by:

$$RePr = (RaPrNu)^{1/3} \times \begin{cases} 2.1(10^{-9}Ra)^{0.004} & (Pr = 0.025,\ 5\times10^6 \leqslant Ra \leqslant 5\times10^9), \\ 1.9(10^{-9}Ra)^{0.057} & (Pr = 0.7,\ 10^8 \leqslant Ra \leqslant 10^{14}), \\ 2.0 & (Pr = 7,\ 3\times10^7 \leqslant Ra \leqslant 4\times10^9), \end{cases} \tag{4.13}$$

The liquid mercury data ($Pr = 0.025$) are taken from Cioni *et al.* (1997); the helium data ($Pr = 0.7$) are from Castaing *et al.* (1989), and the water ($Pr = 7$) data from

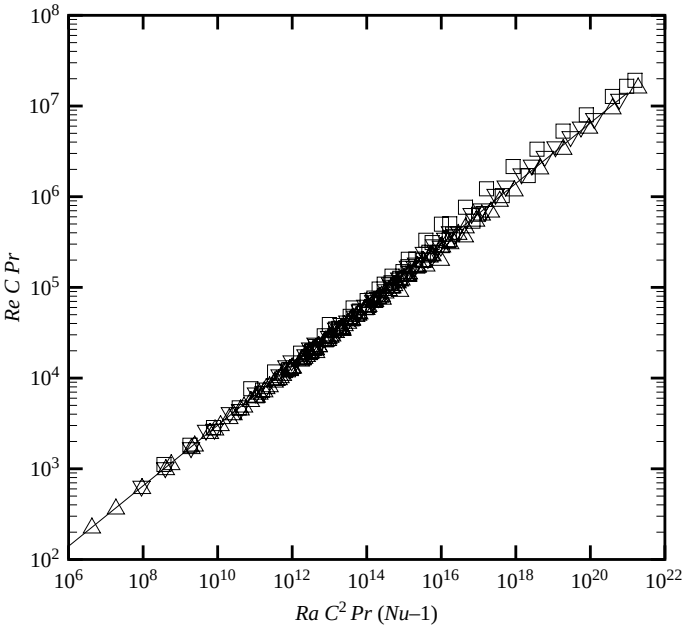


FIGURE 15. The energy conservation relation (4.12) giving the magnitude of the (non-dimensionalized) core velocity fluctuations $Re$. Symbols are simulation results for △, $ZC^2 = 823$; ▽, $10^4$; □, $10^5$. The solid line is (4.12).

Tanaka & Miyata (1980). These experimental results do not all scale identically to the ODT relation (4.12), but the deviations only amount to a few per cent in $Re$ over three orders of magnitude in $Ra$ in the worst case. The experimentally determined constants in the scaling relations indicate that the ODT $Re$ values are about 1/5 of the experimental values (for $C^2 \sim 10^3$), which is good considering the oversimplified nature of the ODT velocity scalar $v$. These experimental results indicate no significant dependence of the prefactor on Prandtl number at $Ra = 10^9$.

The Prandtl-number dependence of $Re$ has been studied in a single apparatus using a variety of fluids to cover the range $3 \leqslant Pr \leqslant 1205$ (Lam *et al.* 2002). Based on the r.m.s. fluctuations of the velocity magnitude in the core, they report that $Re = 0.84Ra^{0.40\pm0.03}Pr^{-0.86\pm0.01}$. Combining this with $Nu = 0.14Ra^{0.3}Pr^{-0.03}$ measured in the same apparatus (Xia *et al.* 2002) gives

$$RePr \simeq 3.2Pr^{-0.18}(RaPrNu)^{1/3}, \tag{4.14}$$

which indicates the prefactor in (4.12) decreases slowly with $Pr$, in contrast to the ODT data. However, the experimental Rayleigh numbers at $Pr \simeq 10^2$ to $10^3$ are much lower than those simulated by ODT, and may not exhibit a fully developed cascade. This would violate the assumptions that led to (4.12), and hence, at higher experimental $Ra$, it is possible that this $Pr$ dependence may weaken and the results become more similar to those of ODT.

The p.d.f. of fluctuations in the value of the ODT velocity scalar in the centre of the cell is shown in figure 16, along with experimental data (for vertical velocity fluctuations) from Daya & Ecke (2001). The data is for $Pr = 5.5$ and $Ra = 2 \times 10^9$, and was collected in both a cylindrical and a square cell (as were the temperature p.d.f.s shown in figure 9). As was the case for the temperature fluctuations, the magnitude

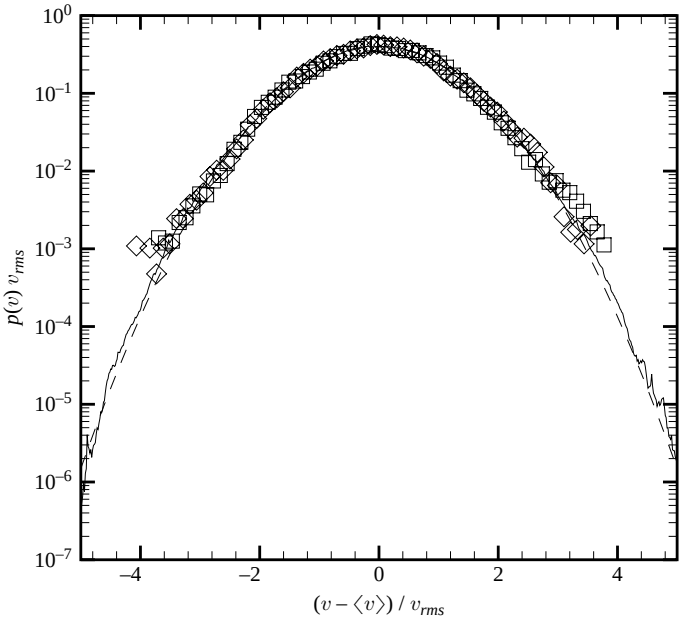


FIGURE 16. Rescaled probability density $p$ of a core velocity fluctuation $v$. ODT simulation data (solid line) for $Pr = 5.5$, $Ra = 2 \times 10^9$ and $ZC^2 = 10^5$. Experimental data from the cell centre in two distinct geometries (□, cylindrical geometry; ◇, rectangular geometry) for the same $Ra$ and $Pr$ are shown for comparison (Daya & Ecke 2001). Also shown is a Gaussian p.d.f. (dashed line).

of the r.m.s. velocity fluctuation $v_{rms}$ used to scale the p.d.f.s is different for the two geometries and for ODT, but the shape of the rescaled p.d.f. appears to be more universal. The shape is nearly Gaussian, as has also been reported in the experiments of Ashkenazi & Steinberg (1999) for $Pr = 93$. Off-centre velocity fluctuation p.d.f.s (not shown) taken at $y = 0.25\Lambda$ and $y = 0.75\Lambda$ showed no significant dependence of the p.d.f. shape on position within the cell core (in contrast to the temperature p.d.f.s).

### 4.4. *Fluctuations in open systems*

To further illustrate the importance of the thermal boundary layers in shaping the core temperature fluctuation p.d.f., ODT simulations were also performed with jump-periodic boundary conditions imposed on $\delta T$ rather than fixed-temperature plates at $y = 0$ and $y = \Lambda$. This eliminates the thermal boundary layer entirely, and the simulation corresponds to an infinitely long unstable temperature gradient. Without plates, there is no natural way to truncate the range of possible eddy sizes in the model, so a largest eddy size equal to the periodicity length $\Lambda$ was imposed. Simulations with Rayleigh numbers in the range $3 \times 10^9 \leqslant RaC^2 \leqslant 3 \times 10^{12}$ were performed for Prandtl number values $Pr = 0.1$, 1.0 and 10, and $ZC^2 = 10^5$. The resulting p.d.f.s had the same shape in all cases; an example is shown in figure 17. The shape is close to a Gaussian, unlike the p.d.f. which results from the simulation with fixed-temperature plates, which is shown for comparison. The deviation from the Gaussian p.d.f. is the result of the mixing of a temperature gradient which extends over many integral scales, as has been observed experimentally by Gollub *et al.* (1991) and Jayesh & Warhaft (1991). This effect has also been seen in stochastic models very similar to the one presented here (Holzer & Pumir 1993; Wunsch 1998), and is arguably a common

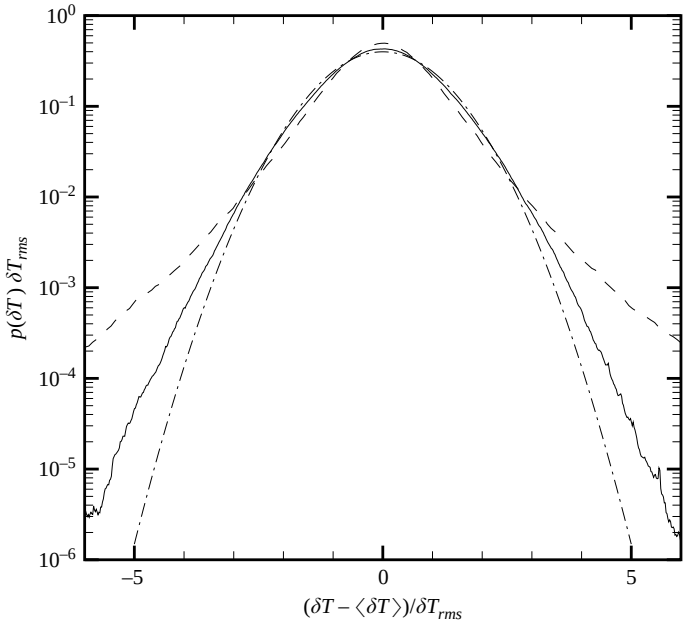


FIGURE 17. Rescaled probability density $p$ of a temperature fluctuation $\delta T$ in an open (periodic) system for $RaC^2 = 3 \times 10^{12}$, $Pr = 1$ and $ZC^2 = 10^5$. The p.d.f. shape (solid line) is very close to a Gaussian (dash-dotted line), but very different from the p.d.f. in a closed (fixed-temperature boundary condition) simulation with the same parameter values (dashed line).

feature of such models in this configuration (Falkovich, Gawedzki & Vergassola 2001). However, the difference between the model p.d.f. in the open and closed configurations demonstrates that this effect of mixing against the temperature gradient is negligible when fixed plates are present, since the p.d.f. in the closed configuration is very non-Gaussian even at small deviations and exhibits a much larger probability of large deviations. This comparison illustrates the fact that the p.d.f.s generated by the model for closed cells are determined by the transport of boundary-layer fluid into the cell interior, and are not an artefact peculiar to models based on stochastic maps.

Heat transfer in this configuration is determined entirely by the large scales. The heat flux is given by $V\Delta T/\Lambda$, where the velocity scale $V$ is given by $V^2 \sim g\Lambda\beta\Delta T/\rho$. Combining these yields $Nu \sim RePr \sim \sqrt{RaPr}$. These scalings correspond to the so-called 'ultimate regime' of thermal convection (Kraichnan 1962). The ODT simulation results are summarized by $Nu = 0.0075C\sqrt{RaPr}$ and $RePr = 0.28\sqrt{RaPr}$. For $Pr = 1$, $Nu \sim Ra^{1/2}$ has also been observed in direct numerical simulations of this configuration by Lohse & Toschi (2003).

The magnitude of the temperature fluctuations $\delta T_{rms}$ should be constant, according to (4.9) with these scalings and $B = 0$. This is not quite true in the simulations, as $\delta T_{rms}/\Delta T$ slowly decreases with increasing $RaC^2$ with a scaling exponent of approximately $0.02 \pm 0.01$. This possibly indicates a weak influence of the molecular parameters ($\kappa$ and $\nu$) on the magnitude of the temperature fluctuations.

### 4.5. *Power spectra*

To study the power spectra in the interior of the one-dimensional domain, spectra were computed using the middle half of the temperature and velocity profiles (with the mean slope subtracted). Spectra from many profiles in each simulation were

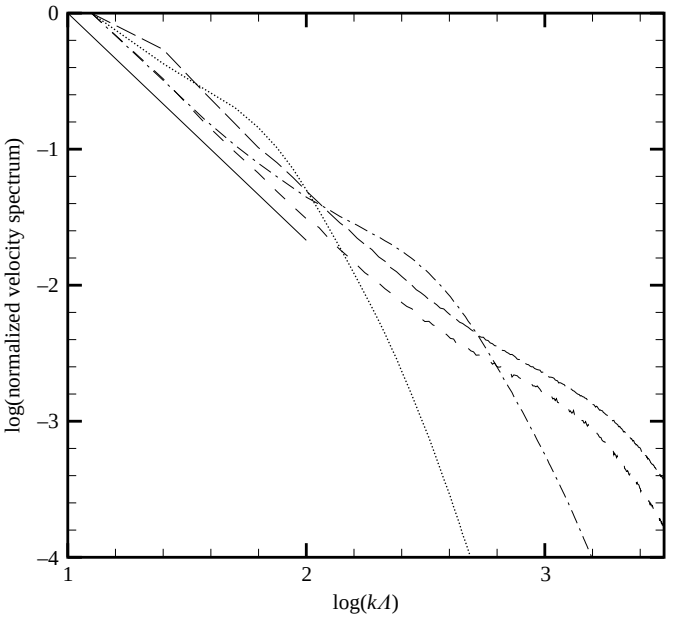


FIGURE 18. Normalized velocity spectra in the centre of the domain for $Pr = 0.025$ (dashed line), $Pr = 0.7$ (dash-dotted line) and $Pr = 1352$ (dotted line), from the highest Rayleigh number simulated for each Prandtl number in the $ZC^2 = 10^5$ set of simulations. Also shown is the expected power law for a Kolmogorov cascade (solid line with slope $-5/3$) and the spectrum from the open (periodic) simulation with $RaC^2 = 3 \times 10^{12}$ and $Pr = 1$ (long-dashed line).

averaged to produce a clean result. Debate continues as to whether the interior of a physical Rayleigh–Bénard cell exhibits a Kolmogorov or a Bolgiano–Obukhov cascade (Siggia 1994; Ashkenazi & Steinberg 1999), but the ODT model appears to choose the Kolmogorov cascade.

Figure 18 shows the velocity spectra for three different Prandtl numbers from the $ZC^2 = 10^5$ set of simulations. For each Prandtl number, the largest Rayleigh number simulation is shown. The spectra have been shifted vertically so as to have the same value at the smallest wavenumber. A line of slope $-5/3$, the scaling exponent expected for a Kolmogorov (kinetic-energy) cascade, is also shown. Both the $Pr = 0.025$ and $Pr = 0.7$ simulations have inertial ranges with slopes which are very close to the Kolmogorov value. The $Pr = 1352$ simulation does not appear to have an inertial range owing to its large viscosity and correspondingly low Reynolds number. Also shown is a spectrum from the open (periodic) system discussed in the previous subsection, which is also consistent with the Kolmogorov cascade. At high wavenumbers, the spectra exhibit a bump, or shoulder, as the inertial range transitions into the dissipative range. This model artefact is due to the transition from eddy mappings to viscous transport as the dominant dynamical mechanism as wavenumber increases. It does not impact the statistical properties of the temperature or velocity fields considered in the previous sections, which depend on the large-scale dynamics of the flow.

Figure 19 shows the temperature spectra for the same simulations as figure 18. In this case, all simulations exhibit inertial ranges with scaling exponents close to $-5/3$, consistent with the Obukhov–Corrsin cascade for a passive scalar.

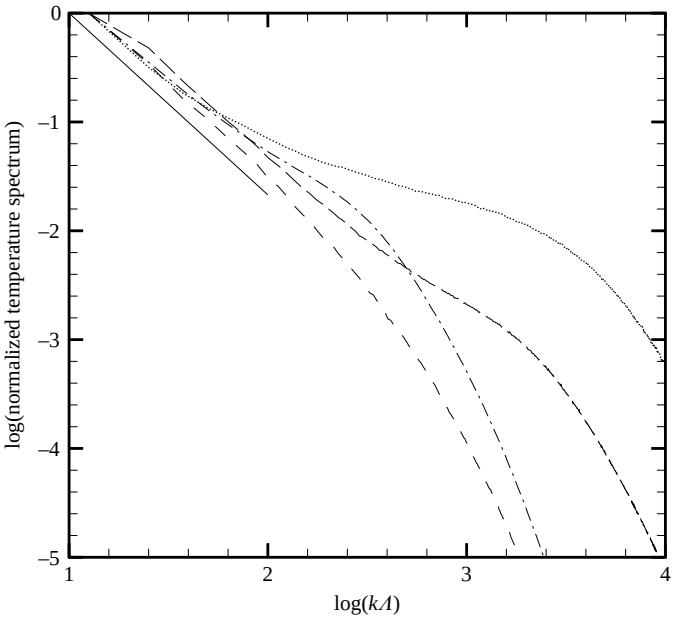


FIGURE 19. Normalized temperature spectra in the center of the domain for $Pr = 0.025$ (dashed line), $Pr = 0.7$ (dash-dotted line) and $Pr = 1352$ (dotted line), from the highest Rayleigh number simulated for each Prandtl number in the $ZC^2 = 10^5$ set of simulations. Also shown is the expected power law for an Obukhov–Corrsin cascade (solid line with slope $-5/3$) and the spectrum from the open (periodic) simulation with $RaC^2 = 3 \times 10^{12}$ and $Pr = 1$ (long-dashed line).

## 5. Conclusions

In this work, a model based on the stochastic application of a mapping function to a one-dimensional domain, with a dynamical rule based on mixing-length arguments, is applied to turbulent convection. Using only two adjustable parameters, the model approximately reproduces heat-transfer rates measured in Rayleigh–Bénard cells over six orders of magnitude in $Ra$ and five orders of magnitude in $Pr$. Although the model does not incorporate some effects which are significant in containers with finite horizontal extent, the model can plausibly be used to study interior fluctuations, and might usefully be applied to natural convecting systems (where sidewall effects are unimportant) in the future.

The present study of temperature fluctuations in the core of a convecting cell demonstrated good agreement between the model and the limited experimental data available for both the overall magnitude of fluctuations and the shape of the fluctuation p.d.f. However, simulations at larger Prandtl numbers and replacement of the fixed-temperature plates at the top and bottom with a jump-periodic boundary condition resulted in significant changes to the fluctuation magnitude and p.d.f. Also, the fluctuation p.d.f. exhibited a strong dependence on vertical location. These results were interpreted using a simple picture in which core fluctuations result from two sources: direct transport of thermal-boundary-layer material into the core with little mixing, and indirect transport, in which boundary-layer material undergoes significant mixing with its surroundings before reaching the core. Changes in the p.d.f. shapes were attributed to shifts in the relative importance of these two mechanisms, and could be observable in large-$Pr$ experiments. Also, a simple mixing-length argument

for the scaling of the magnitude of fluctuations was suggested by this picture and shown to be compatible with the model as well as the available experimental data.

We thank Z. Daya and R. Ecke for helpful comments and for sharing their experimental data. This work was supported by the US Department of Energy, Office of Basic Energy Sciences, Division of Chemical Sciences, Geosciences, and Biosciences.

## Appendix

To illustrate how the assumption of statistical independence of the two contributions to $\delta T_{rms}$ leads to (4.5), we start by writing the random variable $\delta T$ as a sum of two statistically independent random variables denoted $\delta T_1$ and $\delta T_2$. In other words,

$$\delta T \equiv \delta T_1 + \delta T_2. \tag{A 1}$$

Squaring and averaging this definition yields

$$\langle \delta T^2 \rangle = \langle \delta T_1^2 \rangle + \langle \delta T_2^2 \rangle + 2\langle \delta T_1 \delta T_2 \rangle, \tag{A 2}$$

where $\langle \dots \rangle$ denotes an ensemble average, while averaging and then squaring yields

$$\langle \delta T \rangle^2 = \langle \delta T_1 \rangle^2 + \langle \delta T_2 \rangle^2 + 2\langle \delta T_1 \rangle \langle \delta T_2 \rangle. \tag{A 3}$$

The r.m.s. fluctuation $\delta T_{rms}$ of $\delta T$ is defined as

$$\delta T_{rms}^2 \equiv \langle \delta T^2 \rangle - \langle \delta T \rangle^2. \tag{A 4}$$

Substituting (A 2) and (A 3) into (A 4) yields

$$\delta T_{rms}^2 = \left(\langle \delta T_1^2 \rangle - \langle \delta T_1 \rangle^2\right) + \left(\langle \delta T_2^2 \rangle - \langle \delta T_2 \rangle^2\right) + 2\left(\langle \delta T_1 \delta T_2 \rangle - \langle \delta T_1 \rangle \langle \delta T_2 \rangle\right). \tag{A 5}$$

If $\delta T_1$ and $\delta T_2$ are statistically independent, as assumed, then $\langle \delta T_1 \delta T_2 \rangle = \langle \delta T_1 \rangle \langle \delta T_2 \rangle$ and

$$\delta T_{rms}^2 = \left(\langle \delta T_1^2 \rangle - \langle \delta T_1 \rangle^2\right) + \left(\langle \delta T_2^2 \rangle - \langle \delta T_2 \rangle^2\right). \tag{A 6}$$

Now, if we identify $\delta T_{core}$ as the r.m.s. variation of the random variable $\delta T_1$ and $\delta T_{BL}$ as the r.m.s. variation of $\delta T_2$, then

$$\delta T_{core}^2 \equiv \left(\langle \delta T_1^2 \rangle - \langle \delta T_1 \rangle^2\right) \tag{A 7}$$

and

$$\delta T_{BL}^2 \equiv \left(\langle \delta T_2^2 \rangle - \langle \delta T_2 \rangle^2\right). \tag{A 8}$$

Using these, we arrive at (4.5) in the text:

$$\delta T_{rms}^2 = \delta T_{core}^2 + \delta T_{BL}^2, \tag{A 9}$$

which simply says that the mean-square fluctuation of the composite variable $\delta T$ is the sum of the mean-square fluctuations of its two independent components. This does not imply anything about the relative magnitudes of $\delta T_{core}^2$ and $\delta T_{BL}^2$; it is the purpose of the discussion that follows (4.5) to estimate their magnitudes and show that their relative contributions to $\delta T_{rms}$ varies as we consider different values of $Ra$ and $Pr$.

## REFERENCES

Ahlers, G. & Xu, X. 2001 Prandtl-number dependence of heat transport in turbulent Rayleigh–Bénard convection. *Phys. Rev. Lett.* **86**, 3320–3323.

Ashkenazi, S. & Steinberg, V. 1999 Spectra and statistics of velocity and temperature fluctuations in turbulent convection. *Phys. Rev. Lett.* **83**, 4760–4763.

Castaing, B., Gunaratne, G., Heslot, F., Kadanoff, L., Libchaber, A., Thomae, S., Wu, X.-Z., Zaleski, S. & Zanetti, G. 1989 Scaling of hard thermal turbulence in Rayleigh–Bénard convection. *J. Fluid Mech.* **204**, 1–30.

Chavanne, X., Chilla, F., Castaing, B., Hebral, B., Chabaud, B. & Chaussy, J. 1997 Observation of the ultimate regime in Rayleigh–Bénard convection. *Phys. Rev. Lett.* **79**, 3648–3651.

Chavanne, X., Chilla, F., Chabaud, B., Castaing, B. & Hebral, B. 2001 Turbulent Rayleigh–Bénard convection in gaseous and liquid He. *Phys. Fluids* **13**, 1300–1320.

Cioni, S., Ciliberto, S. & Sommeria, J. 1997 Strongly turbulent Rayleigh–Bénard convection in mercury: comparison with results at moderate Prandtl number. *J. Fluid Mech.* **335**, 111–140.

Daya, Z. A. & Ecke, R. E. 2001 Does turbulent convection feel the shape of the container? *Phys. Rev. Lett.* **87**, 184501.

Daya, Z. A. & Ecke, R. E. 2002 Prandtl-number dependence of interior temperature and velocity fluctuations in turbulent convection. *Phys. Rev.* E **66**, 045301(R).

Falkovich, G., Gawedzki, K. & Vergassola, M. 2001 Particles and fields in fluid turbulence. *Rev. Mod. Phys.* **73**, 913–975.

Garon, A. M. & Goldstein, R. J. 1973 Velocity and heat transfer measurements in thermal convection. *Phys. Fluids* **16**, 1818–1825.

Goldstein, R. J., Chiang, H. D. & See, D. L. 1990 High-Rayleigh-number convection in a horizontal enclosure. *J. Fluid Mech.* **213**, 111–126.

Goldstein, R. J. & Tokuda, S. 1980 Heat transfer by thermal convection at high Rayleigh numbers. *Intl J. Heat Mass Transfer* **23**, 738–740.

Gollub, J. P., Clarke, J., Gharib, M., Lane, B. & Mesquita, O. N. 1991 Fluctuations and transport in a stirred fluid with a mean gradient. *Phys. Rev. Lett.* **67**, 3507–3510.

Grossmann, S. & Lohse, D. 2000 Scaling in thermal convection: a unifying theory. *J. Fluid Mech.* **407**, 27–56.

Grossmann, S. & Lohse, D. 2001 Thermal convection for large Prandtl numbers. *Phys. Rev. Lett.* **86**, 3316–3319.

Grossmann, S. & Lohse, D. 2002 Prandtl and Rayleigh number dependence of the Reynolds number in turbulent thermal convection. *Phys. Rev.* E **66**, 016305.

Holzer, M. & Pumir, A. 1993 Simple models of non-Gaussian statistics for a turbulently advected passive scalar. *Phys. Rev.* E **47**, 202–219.

Horanyi, S., Krebs, L. & Muller, U. 1999 Turbulent Rayleigh–Bénard convection in low Prandtl-number fluids. *Intl J. Heat Mass Transfer* **42** 3983–4003.

Jayesh & Warhaft, Z. 1991 Probability distribution of a passive scalar in grid-generated turbulence. *Phys. Rev. Lett.* **67**, 3503–3506.

Kerr, R. M. & Herring, J. R. 2000 Prandtl number dependence of Nusselt number in direct numerical simulations. *J. Fluid Mech.* **419**, 325–344.

Kerstein, A. R. 1999 One-dimensional turbulence: model formulation and application to homogeneous turbulence, shear flows, and buoyant stratified flows. *J. Fluid Mech.* **392**, 277–334.

Kimmel, S. J. & Domaradzki, J. A. 2000 Large-eddy simulations of Rayleigh–Bénard convection using subgrid scale estimation model. *Phys. Fluids* **12**, 169–184.

Kraichnan, R. 1962 Turbulent thermal convection at arbitrary Prandtl number. *Phys. Fluids* **5**, 1374–1389.

Lam, S., Shang, X.-D., Zhou, S.-Q. & Xia, K.-Q. 2002 Prandtl number dependence of the viscous boundary layer and the Reynolds numbers in Rayleigh–Bénard convection. *Phys. Rev.* E **65**, 066306.

Lohse, D. & Toschi, F. 2003 The ultimate state of thermal convection. *Phys. Rev. Lett.* **90**, 34502.

Niemela, J. J., Skrbek, L., Sreenivasan, K. R. & Donnelly, R. J. 2000 Turbulent convection at very high Rayleigh numbers. *Nature* **404**, 837–840.

Roche, P.-E., Castaing, B., Chabaud, B., Hebral, B. & Sommeria, J. 2001 Side wall effects in Rayleigh–Bénard experiments. *Eur. Phys. J.* B **24**, 405–408.

Rossby, H. T. 1969 A study of Bénard convection with and without rotation. *J. Fluid Mech.* **36**, 309–335.

Siggia, E. D. 1994 High Rayleigh number convection. *Annu. Rev. Fluid Mech.* **26**, 137–168.

Takeshita, T., Segawa, T., Glazier, J. A. & Sano, M. 1996 Thermal turbulence in mercury. *Phys. Rev. Lett.* **76**, 1465–1468.

Tanaka, H. & Miyata, H. 1980 Turbulent natural convection in a horizontal water layer heated from below. *Intl J. Heat Mass Transfer* **23**, 1273–1281.

Verzicco, R. & Camussi, R. 1999 Prandtl number effects in convective turbulence. *J. Fluid Mech.* **383**, 55–73.

Verzicco, R. 2002 Sidewall finite-conductivity effects in confined turbulent thermal convection. *J. Fluid Mech.* **473**, 201–210.

Wu, X. Z. & Libchaber, A. 1992 Scaling relations in thermal turbulence: the aspect-ratio dependence. *Phys. Rev.* A **45**, 842–845.

Wunsch, S. 1998 A simple passive scalar advection–diffusion model. *Phys. Rev.* E **58**, 5757–5764.

Wunsch, S. & Kerstein, A. R. 2001 A model for layer formation in stably stratified turbulence. *Phys. Fluids* **13**, 702–712.

Wunsch, S. 2003 Stochastic simulations of buoyancy-reversal experiments. *Phys. Fluids* **15**, 1442–1456.

Xia, K.-Q., Lam, S. & Zhou, S.-Q. 2002 Heat-flux measurement in high-Prandtl-number turbulent Rayleigh–Bénard convection. *Phys. Rev. Lett.* **88**, 064501.